# Developing a Low-Noise Data Acquisition System for Detection of Electric and Magnetic Fields in Seawater

*Presented in Partial Fulfillment of*
*the Requirements for the Degree of*

Master of Science

*with a Major in*

Electrical Engineering

*in the*

College of Graduate Studies

University of Idaho

*by*

Richard Allen Oare

*Major Professor*
Michael Santora, Ph.D.

*Committee*
Michael Anderson, Ph.D.
James Frenzel, Ph.D.

*Department Administrator*
Mohsen Guizani, Ph.D.

August 2016

## Authorization to Submit Thesis

This thesis of Richard Allen Oare, submitted for the degree of Master of Science with a major in Electrical Engineering and titled "Developing a Low-Noise Data Acquisition System for Detection of Electric and Magnetic Fields in Seawater," has been reviewed in final form. Permission, as indicated by the signatures and dates below, is now granted to submit final copies to the College of Graduate Studies for approval.

| | | |
|---|---|---|
| Major Professor: | Michael Santora, Ph.D. | Date |
| Committee Members: | Michael Anderson, Ph.D. | Date |
| | James Frenzel, Ph.D. | Date |
| Department Administrator: | Mohsen Guizani, Ph.D. | Date |

# Abstract

The Office of Naval Research (ONR) has taken an interest in developing a modular electric and magnetic field sensor and acquisition system that can be mounted on a small autonomous underwater vehicle (AUV). In this thesis, a fully integrated data acquisition system is presented, achieving low power dissipation and low cost. Analog signal amplification uses instrumentation amplifiers due to their inherently low noise characteristics, high input impedance, and ease of gain adjustment. Signal conditioning circuitry is used to provide an acceptable voltage range for an analog to digital converter (ADC). A microcontroller is used to connect to the ADC to provide data buffering and retrieval capabilities. Connected to the microcontroller is a low-power microprocessor to handle higher level applications and data storage. In addition, silver-silver-chloride (Ag/AgCl) electrodes are used as the sensors to detect electric fields in seawater.

# Acknowledgements

I would like to thank my major professor, Dr. Michael Santora, for his advice and expertise on this research. I would also like to thank my committee, Dr. James Frenzel and Dr. Michael Anderson, whom I have worked closely with throughout this project. Finally, I am grateful and indebted for the support provided by my family who have been behind every life decision I have made. Without them I would not be afforded the immense opportunities in life that I have been fortunate enough to have.

# Table of Contents

# List of Tables

# List of Figures

CHAPTER 1

# Introduction

This research involves the development of a data acquisition system (DAQ) for use on an autonomous underwater vehicle (AUV) to collect electric field and magnetic field measurements. Included herein is the design, development, testing, and implementation details along with future design improvements. This system utilizes an analog to digital converter (ADC) in conjunction with analog signal amplification and signal conditioning circuitry. Silver-silver-chloride (Ag/AgCl) electrodes are used as the sensors to sense electric fields in seawater. The output of the sensors is attached to analog signal amplification, which uses instrumentation amplifiers due to their inherent low-noise characteristics and ease of gain adjustments. Signal conditioning circuitry provides a voltage range commensurate with the ADC voltage rating. A microcontroller is used to connect to an ADC providing data buffering and retrieval capabilities. The microprocessor connects to the microcontroller and accepts user input for command and control over the microcontroller. Wireless data connection is provided through an ad-hoc 802.11 network created on a Linux embedded operating system with shell scripting, Python, and C programming.

## 1.1 BACKGROUND

The most common ocean electric field measurement usages are for marine geophysical surveys and vessel signature detection. Since seawater acts as a low-pass filter and attenuates signals above 10 $Hz$, focus is on 10 $Hz$ and below [3]. However, signals up to 1 $kHz$ are expected to be detected since the signals of interest are of man-made origin. This research is funded by the Office of Naval Research (ONR) for the development of a small, modular device to measure and store electric field and magnetic field data. Data is offloaded once the AUV has surfaced and post processing can be completed. The AUV used to host the sensor module is shown in Figure 1.1.

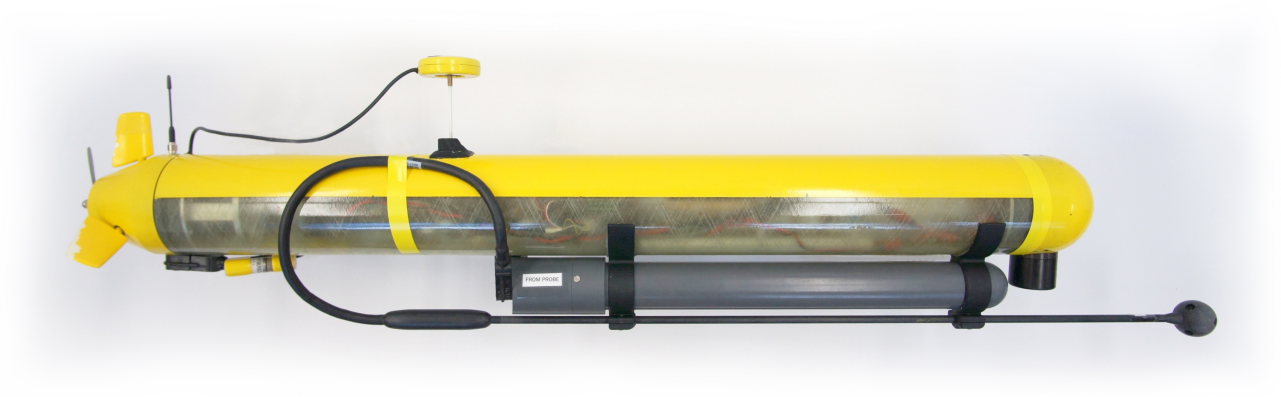

FIGURE 1.1: AUV with a Preamplifier and 1.5-inch Ball Probe Attached

Sources of parasitic electric and magnetic fields exist on vessels. Motors and generators, static fields on the hull of a ship, shaft turning rate, and blade rate all contribute to the signature of a vessel. Methods to counteract these fields include active shaft grounding (ASG), active cathode protection (ACP), and degaussing the hull. Utilizing ASG consists of grounding the bearing of the shaft to the hull of the ship to ensure the potential of the hull and shaft are the same. ACP detects the difference between one point of the ship and another, then actively counteracts the field by actively applying a potential where necessary. These techniques reduce the signature, but do not eliminate it entirely [4].

A proof-of-concept device [5] was developed using a Dexter Research 1010 amplifier with a resistor voltage divider on the output to accommodate the $\pm 1.25$ $V$ range of a 16-bit ADC, internal to the AUV. This system was able to detect a source in the ocean, but many shortcomings were found, including a feedback loop as shown in Figure 1.2. The feedback loop led to instability issues such that the sensor bias became artificially high, causing the output of the amplifier to saturate. This resulted in the ADC reading either the minimum or maximum possible voltage of the ADC. Other devices solve this flaw with high-impedance inputs, between the input and the output, for the sensors providing a virtual disconnect such that further components do not influence the sensor measurements. Use of an instrumentation amplifier provides this high impedance input in a single integrated circuit (IC).

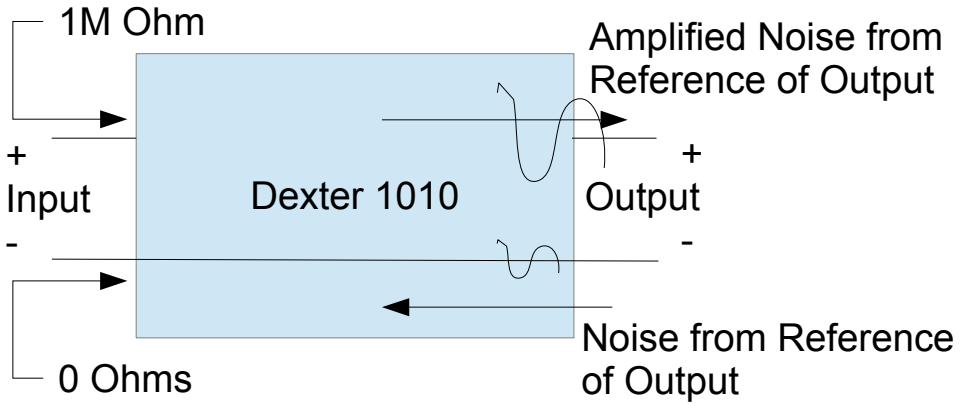


FIGURE 1.2: Dexter Amplifier Feedback Loop

Many groups have developed stationary electric field sensors or moving sensors with tow boats, but there are no known designs for a modular electric field sensing system for use on an AUV. As such, additional complexities are added including flow noise, the need for small form factor, and the ability to deploy and recover the system autonomously. These factors must be balanced to achieve a low power usage, low noise floor, and small form factor.

## 1.2 CONTRIBUTIONS

This document describes the development of a modern, modular data acquisition system for the measurement of electric fields and magnetic fields in seawater. The data acquisition system herein is broken into three distinct subsystems: the sensors for electric fields and magnetic fields in seawater as described in Chapter 2, signal amplification as described in Chapter 3, and the data acquisition recording as described in Chapter 4. Test results and noise measurement details are provided in Chapter 5. Chapter 5 also sets a procedure to ensure consistent electric field noise measurements with the methodology described in Section 5.3. Each chapter provides the technical basis for the hardware or software usage, alternative methodologies, final design, and implementation. Chapter 6 provides the conclusion for each of the chapters presented.

CHAPTER 2

# Detection of Electric and Magnetic Fields in Seawater

## 2.1 INTRODUCTION

Electric field measurements are used for a variety of applications, including medical devices, marine biology, marine geology, and military. With this study, the desired electric field and magnetic field measurements are made with a small autonomous underwater vehicle (AUV) operating in the ocean. Seawater measurements, in particular, have a large degree of difficulty due to the nature of the medium acting as a low-pass filter. This results in a very low noise floor in the ocean, at just a fraction of a Hertz and higher. The complexity of the required instrumentation increases due to the these small-amplitude, low-frequency signals. Amplifiers are well studied and readily available to accommodate these requirements, leaving the sensors as the limiting factor [6; 3].

Two major categories of sensors exist; capacitive, non-contact and resistive, contact sensors. Of these two categories, the resistive, silver-silver chloride (Ag/AgCl), and the capacitive, carbon fiber, electrodes have become the most dominant. Differences are noted when looking at the frequency spectrum. Resistive sensors are used for low-frequency, whereas capacitive sensors perform optimally at mid to high frequencies. The impedance of capacitive sensors increases as the frequency decreases, causing a disconnect between the salt water and the sensors. Resistive sensors impedance remains relatively constant through low frequencies, maintaining the connection between the electrodes [7; 8].

When electric field sensors can be permanently placed in the ocean, separation distance can be used to help achieve a much lower noise floor. Spacing of 1,000 meters has been used to achieve a $10^{-24}\ \frac{V^2}{m^2 Hz}$ noise floor [9], but this spacing is infeasible for a device to be carried by an AUV. In addition to the electric field sensors, magnetic field sensors are used. It is well known that a changing electric field produces a magnetic field, which, for most applications, makes using these sensors in conjunction a rare

occurrence. However, when the electric field sensor separation is limited based on the need for a small-scale AUV to carry the device, sensing of the magnetic field can provide additional assurance that a relevant signal exists. Post processing of the data can use the electric field sensors and magnetic field sensors to validate each other and provide additional information. The sensor used for magnetic field detection, in this work, is the "Model 534 Miniature 3-Axis Fluxgate Magnetometer" made by Applied Physics Systems. This thesis focuses on the electric field sensors since the magnetic measurements have been previously completed with an adequate degree of accuracy [10].

## 2.2 SILVER-SILVER CHLORIDE SENSORS

Silver-silver chloride (Ag/AgCl) sensors work by a reversible reaction of separation and recombination of the silver from the chloride to produce an electron [11]. These sensors are resistive sensors, requiring a contact with saltwater to form a salt bridge across a pair of sensors. This salt-bridge across the sensors develops a potential, in the presence of an electric field, that can then be detected by instrumentation. Sensors of this kind have superior low-frequency characteristics than their non-contact counterparts. Since seawater has a large attenuation above a fraction of a Hertz, Ag/AgCl sensors are preferred for oceanic electric field sensing. In addition, larger Ag/AgCl sensors inherently have a higher signal-to-noise ratio (SNR) due to a larger surface area for detection of the electric field [3].

### 2.2.1 *Characteristics of Sensors*

When the sensors are moved from air to saltwater the electrodes take an estimated 90 minutes to settle such that accurate data can be obtained. The settling time test data is provided in Section 5.6.3. After the settling time, the sensors can remain stable in the seawater for years. The Ag/AgCl also naturally deters buildup of bio-organisms, allowing the sensors to be less affected by micro-organisms [8]. For AUVs, this is necessary to ensure sensor quality such that they can be used many times.

### 2.2.2 *Probe Designs*

Two major designs are developed for use on a small-scale AUV, one being a ball probe, as displayed in Figure 2.1, and the other mounts sensors directly on the hull, as shown in Figure 2.2. A ball probe sensor fixes the electrodes at a known, set distance apart. This separation distance is equal with all three pair directions such that the noise per meter can be calculated equally. Hull mounted sensors on the other hand vary with the different three pair separations. The hull mounted sensors suffer from a series of technical issues such as differing wire lengths to each pair of sensors, long lead wires, need for assembly and disassembly, and other variabilities from one test to another. For these reasons, the hull mounted sensors are not considered due to the high degree of variation between each test case and each AUV set of sensors. In contrast, the ball probe is fixed with tightly controlled parameters, such as permanently mounted sensors and short input wires to the amplifier on the 3-inch model.

FIGURE 2.1: Ball Probe Configuration: 1.5-inch and 3-inch diameter

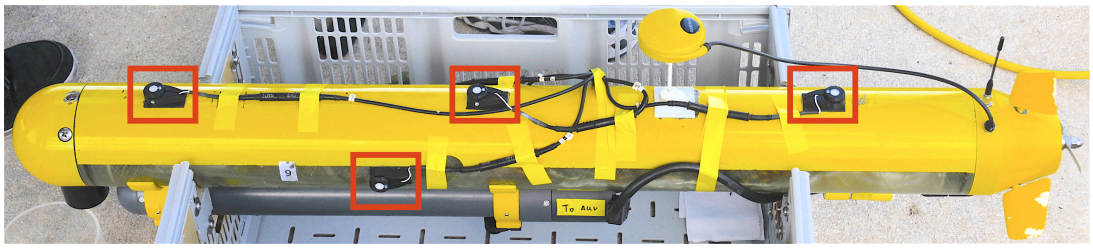

FIGURE 2.2: Hull Mounted Electrode Configuration (Red Boxes Highlight Electrode Locations)

BALL PROBE — Two different diameter ball probes are developed, one being one and a half inches and the other being three inches, as shown in Figure 2.1. The 3-inch ball probe incorporates the preamplifier within the probe, as shown in Figure 2.3, such that the distance from the preamplifier to the sensors is minimized. Basis for the development of the 3-inch ball probe stems from the electrode manufacture estimated average noise, of 1 $\mu V_{PP}$ on electrode pairs [12]. This estimated noise from the manufacture along with the desired specifications for a 5 $\frac{\mu V_{RMS}}{m}$ noise floor resulted in the development of an estimated noise floor as a function of ball probe diameter, as shown in Figure 2.4.

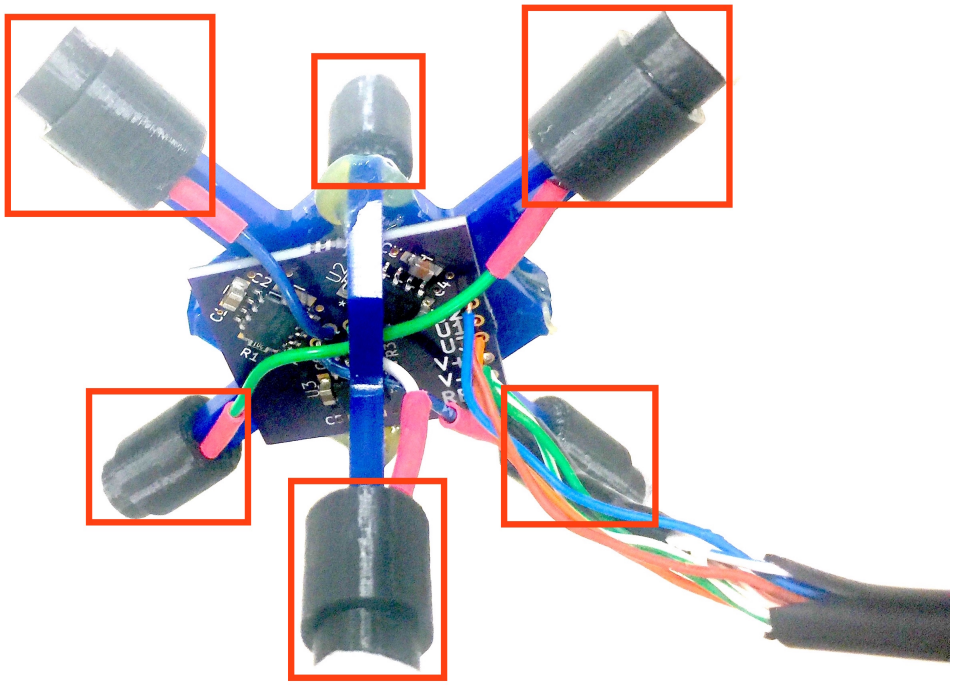

FIGURE 2.3: Inside of the 3-inch Ball Probe (Before Liquid Polymer is Applied)

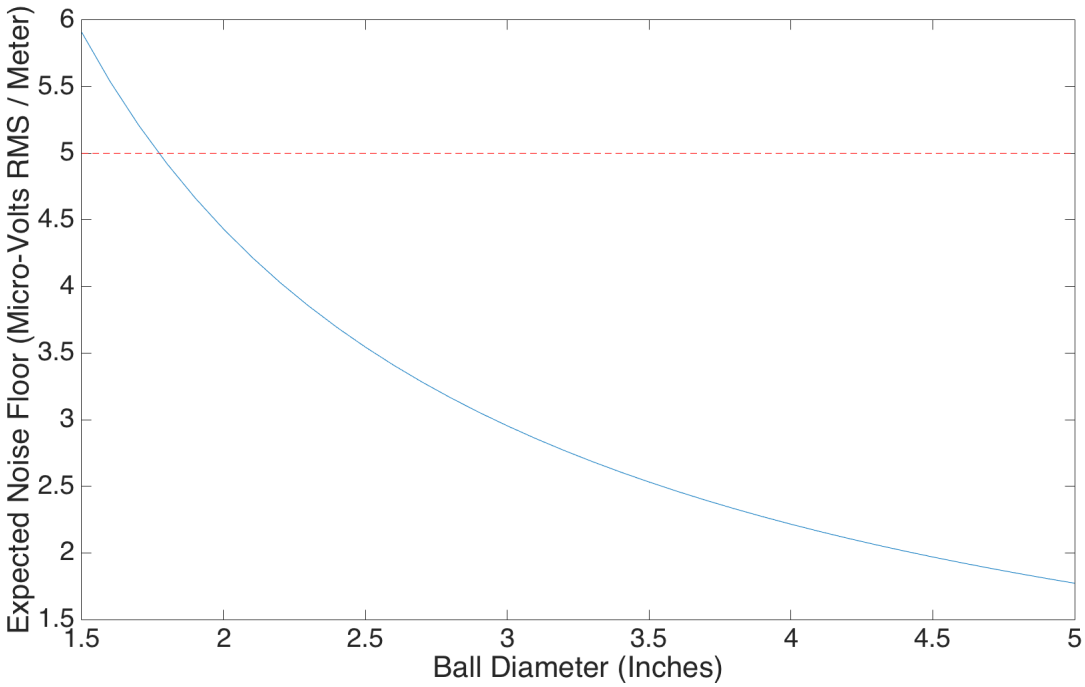


FIGURE 2.4: Estimated Noise Per Meter of Electrode Separation

Manufacturing of the 1.5-inch ball probe requires placing the electrodes in a fixture, shown in Figure 2.5. This fixture is then closed and a liquid polymer is poured into the mold. The 3-inch ball probe uses an alternative fixture, as shown in Figure 2.6, to fix the electrodes and amplifier in place. The fixture is then capped, at each electrode, and pressed against the sides of the mold with a foam seal. This fixture method creates an air pocket, around the electrodes, to protect the electrode surface from being covered by the liquid polymer. Both ball probes use a fiberglass rod to run the wires through and provide a mechanism to mount the ball probe to the AUV. Further construction details are provided in Appendix B.

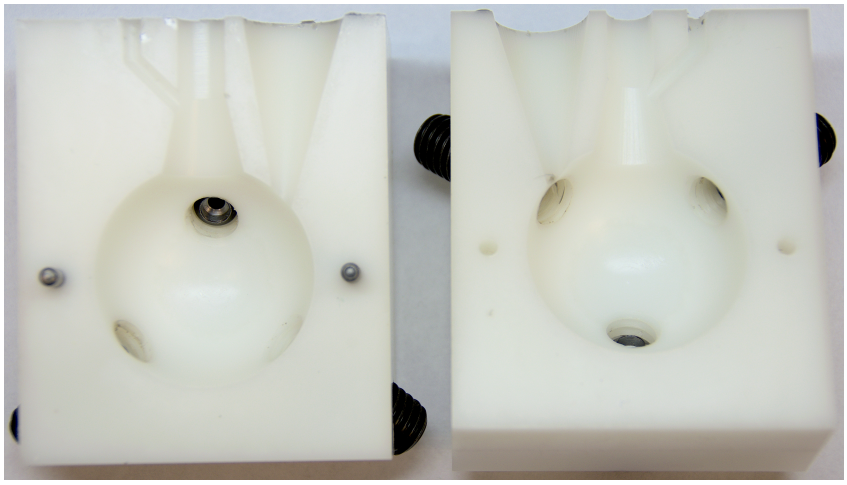

FIGURE 2.5: 1.5-inch Ball Probe Mold (Both Sides Pictured Open)

FIGURE 2.6: 3-inch Ball Probe Mold

Another 3-inch ball probe is developed, as shown in Figure 2.7, utilizing 12 *mm* diameter disc electrodes. This is an increase of surface area in contact with the seawater in comparison to the 3-inch ball probe using cylindrical electrodes. The purpose is to increase signal-to-noise ratio (SNR) while maintaining a low noise floor. Further details on the SNR measurement can be found in Section 5.7.

FIGURE 2.7: 3-inch Ball Probe Utilizing 12 *mm* Diameter Disc Electrodes

HULL MOUNTED — Hull mounted electrodes mount the electrodes into a fixture attached to the hull of the AUV as shown in Figure 2.2. This design increases the separation distance, but at the cost of varying the separation distances among the different directions and more variation in other parameters. These parameters include variations in electrode separation from one AUV to another and that an electrode may not be in the same place from one data collection set to the next. The separation distance issue stems from the fixture being glued to the hull of each AUV, but measurement errors may exist from one AUV to another. Care must also be taken to ensure the same sensor is placed in the same position on the hull (eg. front to back vs back to front) to ensure consistency between measurement sets. Additionally, mechanical stress is added when the electrodes are placed and taken out such that the solder joint may break.

### 2.2.3 *Addition of Agar Solution*

Agar is commonly used to slow the rate at which the Ag/AgCl dissolves and provides a high concentration of chloride at the surface of the electrode [13]. Essentially, the

agar acts as a low-pass filter and a protectant to the electrodes. Once agar is applied, the electrodes must remain in water to keep the agar from drying. Agar must be removed if the electrodes are to be stored dry. Additionally, a porous glass frit may be used in conjunction with the agar. The purpose is to ensure the agar remains in place and oceanic life does not pull it out of place. The glass frit provides little value if the duration of agar usage is expected to be short.

## 2.3 NOISE CHARACTERISTICS

The 1.5-inch ball probe suffers from noise incurred on the long lead wires, acting as an antenna, going from the electrodes to the amplifier. An example of this noise is described in Appendix E. This can be attenuated by submerging the amplifier and ball probe, but a better solution is the usage of the 3-inch ball probe containing an amplifier. Having the amplifier close to the electrodes ensures short lead wires to the amplifier and decreases variability by solidifying everything in one placement. Further details are given in Chapter 5.

CHAPTER 3

# Signal Amplification

## 3.1 INTRODUCTION

Since electric fields in the ocean are influenced by the low-pass nature of seawater, the signals of interest are generally of a very low frequency, but not always. The electric field probe, using the silver-silver chloride (Ag/AgCl) sensors, provides a very low amplitude signal. This voltage is typically in the range of microvolts to millivolts. Additionally, the amplifier needs to have high input impedance such that the circuitry does not create a feedback loop that can influence the measurements. These design requirements develop the need for an amplifier with high gain, high input impedance, and low noise in the low frequency range. Two amplification techniques are widely available to meet these requirements. One type is the instrumentation amplifier and the other is the autozero amplifier. Autozero amplifiers are used to decrease the $1/f$ noise of conventional amplifiers. These amplifiers can also be used in an instrumentation amplifier configuration.

High frequency transmission, including 1 $GHz$ through seawater has been performed and can be detected [14]. Man-made signals are the signals of interest, so high frequencies are not ignored, but frequencies of 1 $kHz$ and less are the signals of interest. The maximum frequency used for this research is 2.5 $kHz$ due to the expected man-made signal sources. Ship electric fields are produced from motors, galvanic corrosion, poorly filtered power supplies, the propeller, and other sources. These systems produce an electric field which can be used to detect the signature of a particular ship. Electrochemical potentials build on the hull of ships when exposed to seawater. These potentials are of very small amplitudes. This leads to the need of signal amplification and signal conditioning to more accurately detect these signals. This amplifier must work well in the range between dc and 1 $kHz$.

## 3.2 AMPLIFICATION TECHNIQUES

In order to achieve the low-noise, low-frequency, high-gain characteristics desired, two techniques exist to assist development. One method is to use an instrumentation amplifier and the other is to use an autozero, also known as chopper-stabilized amplifier. Autozero amplifiers can be used in conjunction with instrumentation amplifiers to improve low-frequency to DC noise characteristics.

Instrumentation amplifiers and chopper amplifiers are commonly used for these type of measurements. One study utilized a chopper amplifier for a very-low-noise seawater electric field measurement device, achieving 0.6 $\frac{nV}{\sqrt{Hz}}$ [11]. A thesis study developed an instrumentation amplifier for echo cardiogram (ECG) applications [15]. These amplification techniques are best suited for small-amplitude signals where precision is needed.

### 3.2.1 *Instrumentation Amplifier*

Instrumentation amplifiers are well known to provide high input impedance and easy gain adjustments with a single resistor. The instrumentation amplifier consists of three operational amplifiers (op-amps). Two op-amps are used in a non-inverting configuration then connected to a differential amplifier to take the difference. This configuration is shown in Figure 3.1. Having this configuration allows the amplifier to have inherently high input impedance. Additionally, this allows for a dual supply configuration and built-in signal conditioning due to the supply rails on the op-amps being separate from the 'ground' reference node.

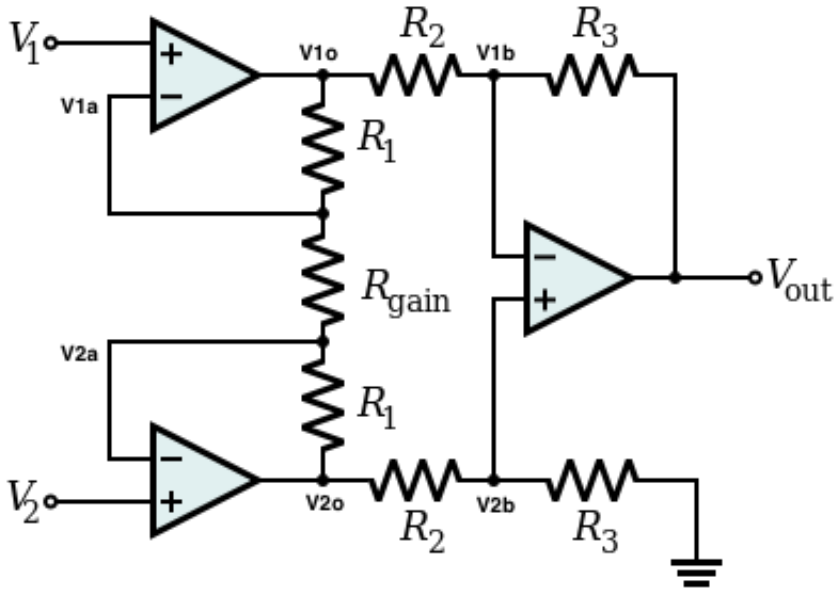


FIGURE 3.1: Basic Instrumentation Amplifier [1]

### 3.2.2 *Autozero (Chopper Stabilization)*

The goal of this method is to reduce or eliminate the offset voltage of the operational amplifier itself. Amplifier noise, especially $1/f$ noise, is essentially eliminated using these techniques and a flat spectral response at low-frequencies can be demonstrated [16]. The noise however, is turned into a broadband white noise, thus raising the noise floor in comparison to common op-amps. One methodology is to autozero the signal using two operational amplifiers (op-amps). One op-amp is used to amplify the signal while the other is used to null the offset voltage of itself and the signal amplifying op-amp separately. This design is shown in Figure 3.2. This amplifier changes switch $s1$ and $s2$ at the same time such that the op-amp $U1$ becomes properly offset, with a shorted input, then switches to $U2$. The offset voltages are stored on capacitor $C1$, for op-amp $U1$, and capacitor $C2$, for op-amp $U2$.

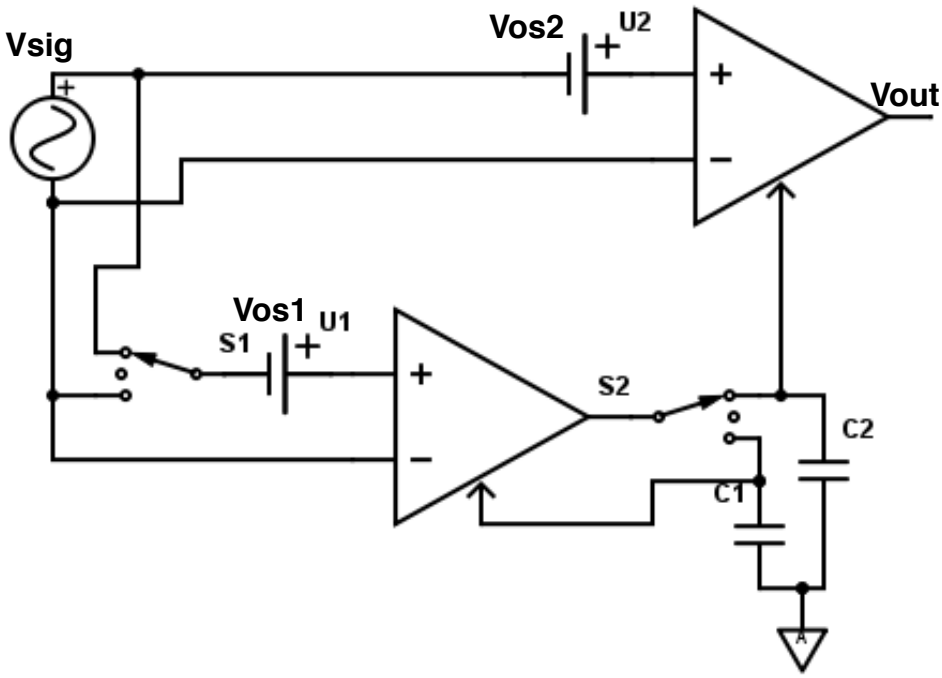


FIGURE 3.2: Basic Autozero Amplifier

## 3.3 DESIGN

Usage of an instrumentation amplifier is essential for obtaining the necessary bipolar voltage swing. Since this is to be used on an AUV where typical runtime is less than an hour, a small number of samples will be collected. With a small number of samples, it may not be feasible to accurately average enough samples in the ultra-low frequencies where chopper stabilized or autozero amplifiers have their advantages. With this, a list of available instrumentation amplifiers is developed and the Texas Instruments INA129 is chosen.

It is desired to have an amplifier capable of producing a noise floor around the estimated noise floor of the electrodes, at 1 $\mu V_{PP}$. The INA129 has an estimated noise floor of 0.2 $\mu V_{PP}$ in the frequency band of 0.1 $Hz$ to 10 $Hz$ [17]. This noise floor rivals the specifications for a number of chopper instrumentation amplifiers, but a chopper amplifier trades the low-frequency noise for a broadband noise, thus raising the overall noise floor.

A printed circuit board (PCB) based on the INA129 is developed, shown in Figure 3.3, with three channels such that all three axis can utilize the same voltage rails.

This PCB measures approximately 1 $inch^2$. Proper design practices are taken into consideration, such as: the usage of power planes, ensuring short traces, ensuring equal length traces for differential inputs, and usage of capacitors for power storage and smoothing.

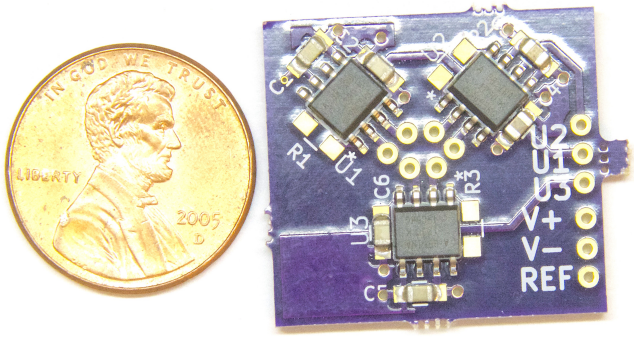


FIGURE 3.3: Three Channel INA129 Printed Circuit Board (PCB)

An autozero instrumentation amplifier circuit based on the Texas Instruments INA333 is developed as shown in Figure 3.4. This can be used in the case where higher runtime ensures enough low frequency samples for accurate measurements. This amplifier combines the benefits of the instrumentation amplifier with the benefits of the chopper amplifier to give superior performance at ultra-low frequencies. Higher frequencies are expected to be affected with a higher noise level.

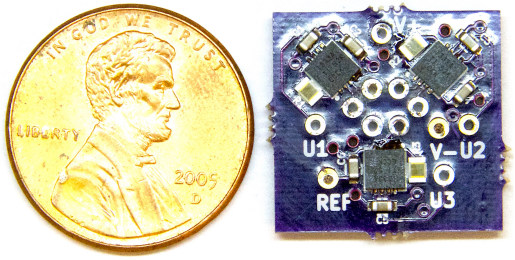


FIGURE 3.4: Three Channel INA333 Printed Circuit Board (PCB)

### 3.3.1 *Gain*

Both amplifier designs are set to as close of a gain of 250 as possible. The INA129 follows the gain of Equation 3.1 as given in the corresponding reference manual, while the INA333 follows the gain of Equation 3.2 as given in the corresponding reference

manual. Table 3.1 gives the minimum and maximum gains for each amplifier design based on a 0.01% resistor and the gain error listed in the reference manuals [17; 18]. A resistor value of 402 Ω is used for the INA333 and the INA129 uses a resistor value of 200 Ω; This results in an expected gain of 249.8 for the INA333 and 248 for the INA129.

$$Gain = 1 + \frac{49.4\ k\Omega}{R_G} \tag{3.1}$$

$$Gain = 1 + \frac{100\ k\Omega}{R_G} \tag{3.2}$$

TABLE 3.1: Range of Actual Expected Gain with Set Gain of Approximately 250

| | Minimum | Maximum |
|---|---|---|
| INA129 | 245.5 | 250.5 |
| INA333 | 248.5 | 251.0 |

## 3.4 NOISE CHARACTERISTICS

Accurate noise measurements have not been obtained due to the very low noise of the amplifiers. This is characterized in Section 5.6.2 where the noise floor is found to be approximately the noise floor of the data acquisition device used to measure.

CHAPTER 4

# Data Acquisition System[1]

## 4.1 INTRODUCTION

A data acquisition system (DAQ) is required to record and store signals collected from the electric field and magnetic field sensors. This DAQ must exhibit low-noise, low-power, and small physical size to operate as a stand-alone system that can be attached to any autonomous underwater vehicle (AUV). It is also desired that this DAQ have a wireless connection to the user and the ability to program the DAQ with a series of sample sets consisting of variables for number of samples, sample rate, and gain. It is desired that these sample sets reside in volatile memory such that a loss of power removes all information associated with how the samples are collected. Creating sample sets in this manner provides a level of security that obfuscates the stored data, requiring knowledge of the parameters which were used to take the samples.

Development of data acquisition systems is widespread for a number of applications. One group in particular developed an hourly updating DAQ for renewable energy monitoring. This group developed a specialized platform with a small microcontroller connected to Radio Frequency (RF) circuitry to forward the information to a basestation connected to a computer using LabView [20]. Another group developed a wireless DAQ, based on the one previously mentioned, for monitoring of photovoltaic arrays and a water pump [21]. Alternatively, another group developed a DAQ using solar power and a wireless RF link to a base station for agricultural monitoring [22]. Similarly, a greenhouse monitoring device was created based on ZigBee wireless technology integrating a temperature sensor, humidity sensor, light sensor, and other sensors [23]. Each of these systems have relatively large development costs in that they are typically made for one specific purpose. These development costs can be recovered when considering the number of units needed and the need for continuous transmission and usage. However, they are specialized to perform a certain task very

[1] Portions of this chapter are adapted from "Modular Low-Power, Low-Noise, Low-Cost Wirelessly Networked Data Acquisition System", published in: OCEANS 2016 - MTS/IEEE [19].

well. Compromises can be made in power usage and hardware cost in order to make systems more modular and applicable to multiple tasks.

Software development cost is another consideration; software needs to be easily modifiable to adapt to new algorithms and new purposes. Using an embedded operating system enables much of the lower level interfaces to be ignored, leaving the application level software as the focus for the developer. Additionally, the graphical interface can be made as a website where Common Gateway Interface (CGI) scripts can control the processes. Ideally, this system can be attached to different analog boards to perform data acquisition tasks for renewable energy, vehicles, or other platforms with simple application level software modifications and appropriate hardware attachments. This requires an Internet of Things (IoT) approach to develop a wireless system for multiple applications.

Data security and integrity is another key aspect to these systems. Many systems even prioritize security and privacy over performance, reliability, and management. It is desired to create a system that can collect data, but if the physical system becomes lost, the data will be unknown to other entities. Security is implemented on this DAQ such that the user can input the desired sampling rates, gain for the sample, and number of samples. This DAQ will then record the samples in the manner the user specifies, only storing the user specifications, in volatile memory until no longer needed. Additionally, commands should be developed to allow the user more interaction with the DAQ.

## 4.2 HARDWARE

An Intel Edison is used as the microprocessor to control the wireless interface along with storing recorded data. Connected to this device, through $I^2C$ is an interface microcontroller (Atmel Atmega328) which controls timing and provides an SPI link to the analog to digital converter (ADC). The ADC is a Texas Instruments (TI) ADS1263 32-bit 38,000 samples per second (SPS) device. Analog circuitry is also used for signal conditioning before being recorded by the ADC. Data is stored on an SD card until sampling is complete and data can be retrieved. A 32 $GB$ SD card can hold roughly

$\frac{32\ GB}{38000 \times 5(\frac{Bytes}{Second})} = 46.8\ Hrs$ of data. This is more than adequate due to the longest expected use of the AUV being roughly 6 *Hrs*. Data can be retrieved through the WiFi interface by connecting to a basestation consisting of a laptop in ad-hoc configuration. The overall system connection diagram is shown in Figure 4.1.

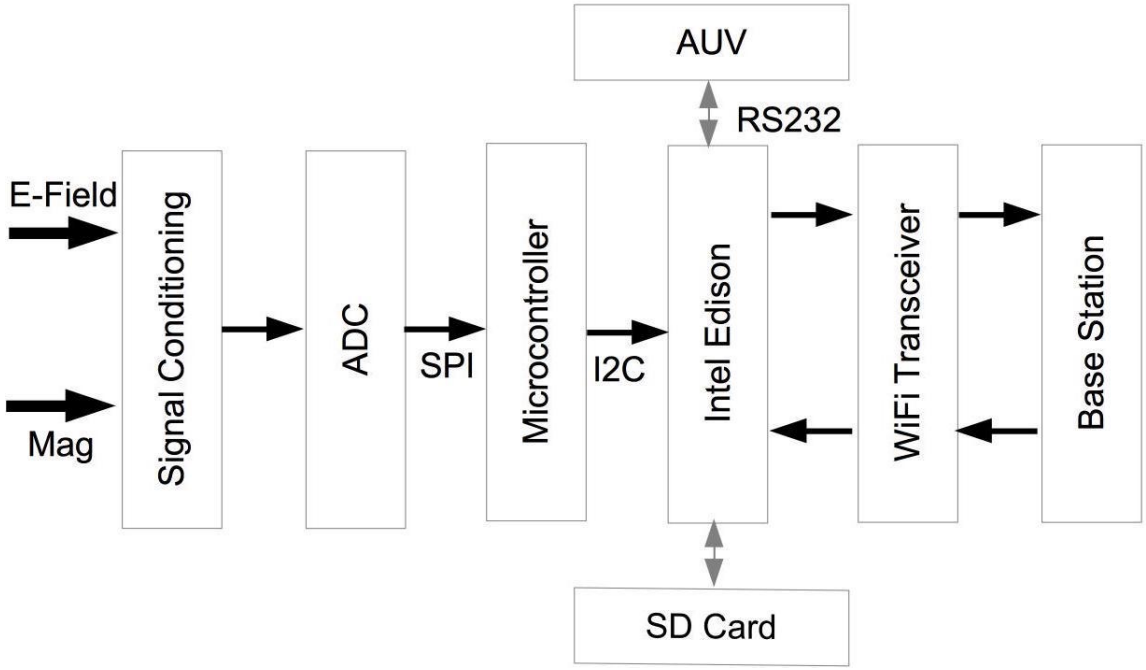


FIGURE 4.1: Hardware Flow Diagram

The Intel Edison is chosen due to its small physical size, low power usage, and adaptability. The Intel Edison is a dual core system running an embedded operating system, Ubilinux, based on Debian Linux. Intel Edison is the successor to the Intel Galileo and both are known to be widely used in IoT applications. The Intel Edison integrates a Bluetooth and WiFi device. For this application, the WiFi device is used for communication, even though the power usage is higher than Bluetooth. Bluetooth can be used as an auxiliary communication device, but the power usage from the wireless device is not a major concern since all wireless devices shut off upon obtaining instructions for data collection. Power usage is found to be approximately 0.77 *W* with the WiFi on and 0.49 *W* with the WiFi off.

The Atmel microcontroller is chosen due to its high user knowledge base, longevity of the device availability, and ease of use. This device provides realtime sampling and data buffering. This alleviates the task of accurate time keeping and ADC commu-

nication from the Intel Edison. Additionally, the Intel Edison utilizes a scheduler in Linux which manages multiple tasks, but does not allow for truly deterministic timing. Making use of the Atmel ensures a modular design by allowing division between each subsystem.

The ADC is chosen due to its sample rate being adequate to satisfy Nyquist on all six channels, low noise, and high resolution. This device includes four extra channels such that another sensor device may be added in the future. Additionally, signal conditioning circuitry is added to accommodate the 1.5-inch or 3-inch ball probe by allowing signal amplification and/or signal conditioning on the DAQ. Utilizing the INA129 instrumentation amplifier keeps the amplifier the same as the 3-inch ball probe in the case where it is used to provide both amplification and signal conditioning.

By configuring the hardware this way, changes can be made to any of the subsystems with minimal changes necessary to the rest of the hardware or software. An example of this would be the usage of a different ADC might affect the subsystems on either side, but no changes would be necessary outside the scope of the ADC. Providing a level of abstraction allows the design to be easily modified into more or less complex systems while maintaining the subsystem approach. Additionally, this improves maintainability since problems can be isolated and fixed much more easily than a non-modular design.

Two versions of this hardware are developed. The first one measures 121 $mm \times 66\ mm$ while the second measures 60 $mm \times 42\ mm$, resulting in a footprint under 4 $in^2$. This size requires a cylindrical container internal diameter of at least 2 $in$, assuming a total board height of 1 $in$. The second version of the hardware, shown in Figure 4.2, can be created for a cost under $200. A Bill of Materials (BOM), itemizing the cost of each component for the DAQ, is included in Appendix D.

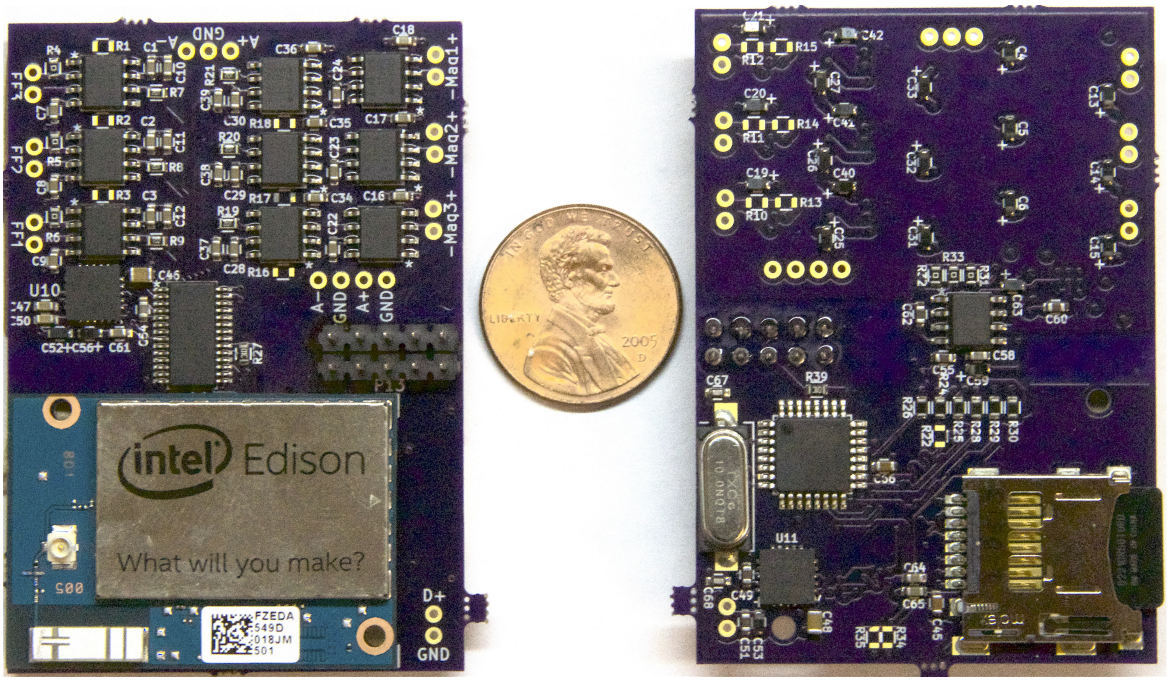


FIGURE 4.2: DAQ Hardware (Front and Back Sides Pictured)

The hardware is composed of six subsystems: The analog sensor inputs, the ADC, the interface microcontroller, power management, the Edison, and the SD card reader. Appendix A contains the schematic for the hardware. Analog sensor inputs consist of signal conditioning to take the input and turn it into a voltage range suitable for the ADC. The interface microcontroller provides a link between the ADC and the Intel Edison. Power management provides appropriate voltage levels to the analog part of the ADC and the input power on the Intel Edison. The Intel Edison hardware provides appropriate connectivity and voltage levels to the Edison module. Lastly, SD card reader circuitry provides appropriate level shifting to the SD card from the Intel Edison and a holder for a microSD card.

## 4.3 SOFTWARE

Software is implemented using a combination of Linux shell scripting, C code, and Python code. For processes with strict timing requirements, C code is used. Other parts, such as the web server, are implemented in Python. This methodology is consistent with design strategies used in the development of Internet of Things (IoT)

devices. Utilizing a resource rich device such as the Intel Edison, power consumption is increased, but development time is decreased and adaptability is increased.

The software for the Intel Edison is developed in the Ubilinux Linux environment. The base station needs to be capable of setting up an ad-hoc wireless network using 802.11 b/g, which is freely available through the use of Linux and Hostapd. After this has been initialized, each Edison on the network must be manually assigned a unique identifier, in this case a static IP address is used, to distinguish between each system. This is set up through the standard Linux wireless device configuration. Python is then used to create and run the web interface. A shell script is used to run the Python webserver upon startup of the system. Common gateway interface (CGI) scripts are then run as an intermediate layer between the webserver and the system to facilitate lower level functionality. Furthermore, lower level interfaces are controlled through a combination of C code and Python. Python is used to control the command structure and facilitate overarching program flow. This includes executing the command structure appropriately and ensuring execution of the C code to send sample set information to the Atmel microcontroller.

### 4.3.1 *Microcontroller Software*

A C program on the Intel Edison interfaces with the Atmel to read data, recorded from the ADC, and store it to a file on the SD card. This program, on the Intel Edison, is made to be called directly from the main Python module. The main Python module can communicate with the C program and supply all of the sample specifications as a Python list along with which channels to read from.

The Intel Edison sends all of the sampling set information to the Atmel, consisting of sample rate, number of samples, and ADC channels to sample. After sampling begins, the Intel Edison waits a set number of expected sample periods then requests the number of samples that have been collected from the Atmel microcontroller. Samples are then collected by the Intel Edison and this routine of requesting the number of samples and obtaining those samples from the Atmel is repeated until the operation is complete. If the Intel Edison requests the number of samples too early, the atmel may return zero as the number of samples available. If the Intel Edison is late in

requesting the number of samples, the atmel will buffer more than expected and return the number of samples available. This reduces time spent keeping the $I^2C$ line busy and ensures accurate sample rate operation. Additionally, to ensure a modular design, a library is made such that a change of ADC will necessitate an update to the library, but nothing more. The ADC library is contained in the Atmel code of the acquisition system.

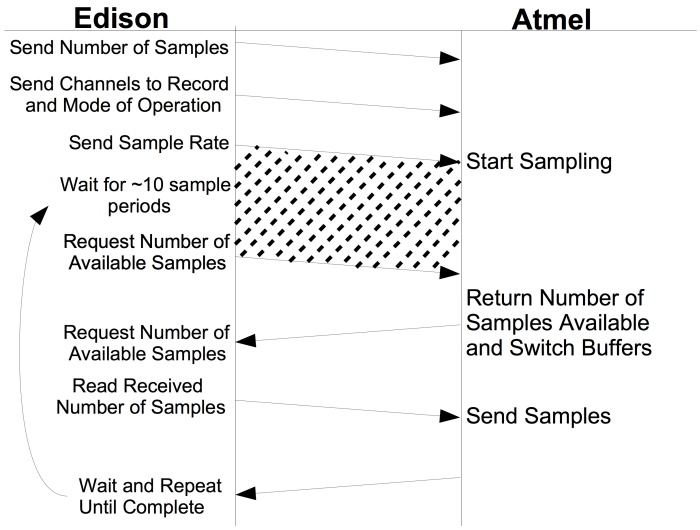


FIGURE 4.3: Atmel to Edison Program Flow

The microcontroller waits until sampling set is received then acts upon the information received. That is, it sets the register on the ADC to the supplied sample rate, it sets a variable for number of samples, and it sets a timer to ensure the correct sample rate. The ADC rate supplied to the microcontroller must be higher than the actual sample rate to ensure correct operation. For each sample, a sample is started, then the ADC interrupts the microcontroller on a pin when the sample is complete. After this occurs, the timer expires and interrupts the microcontroller and the sample is read. After the sample is read, the channel is changed, the number of samples variable is decremented, and the start of conversion is sent to start the next ADC sample. The program flow is shown in Figure 4.4.

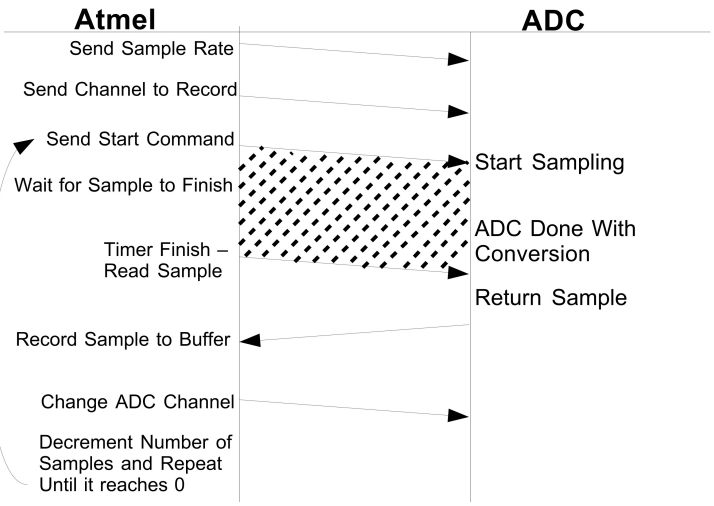


FIGURE 4.4: Atmel to ADC Program Flow

DATA INTEGRITY — A cyclic redundancy check (CRC-8) is implemented to ensure accurate transmission of data on the $I^2C$ line between the Intel Edison and the Atmel microcontroller. This part of the software is adapted from open source C code.

### 4.3.2 *Edison Software*

Three distinct software packages are implemented. One, written entirely in Python, controls the web server and directs the user input for operations such as downloading previously collected signal data and accepting user input. The second part, the Python CGI scripting, validates user input prior to being initialized as a set of instructions. The third part, written in C, provides command and control for the sampling, data recording, and communication with the microcontroller.

WEBSERVER — Linux shell scripting is used to start the webserver upon startup of the system. The shell script calls a Python program to host the webserver as shown in Figure 4.5. The user can input data per the instructions listed on the page and in this document. After the submit button is selected, a CGI script takes over to ensure valid data then execute the program according to the user instructions. The user may also go to the data tab and a CGI script is executed to display the data as shown in Figure 4.6.

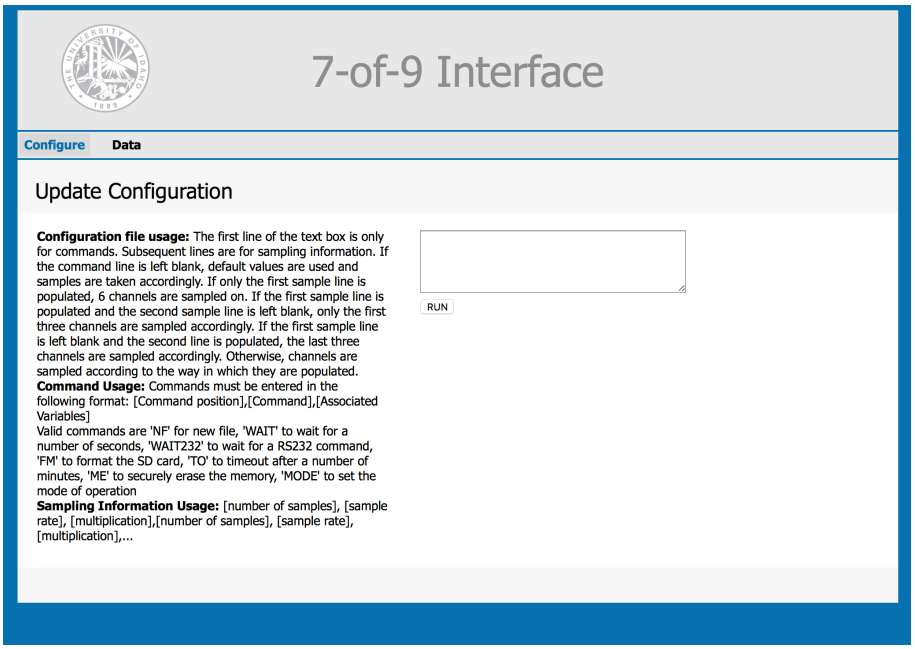


FIGURE 4.5: Main Webpage for User Entry of Parameters

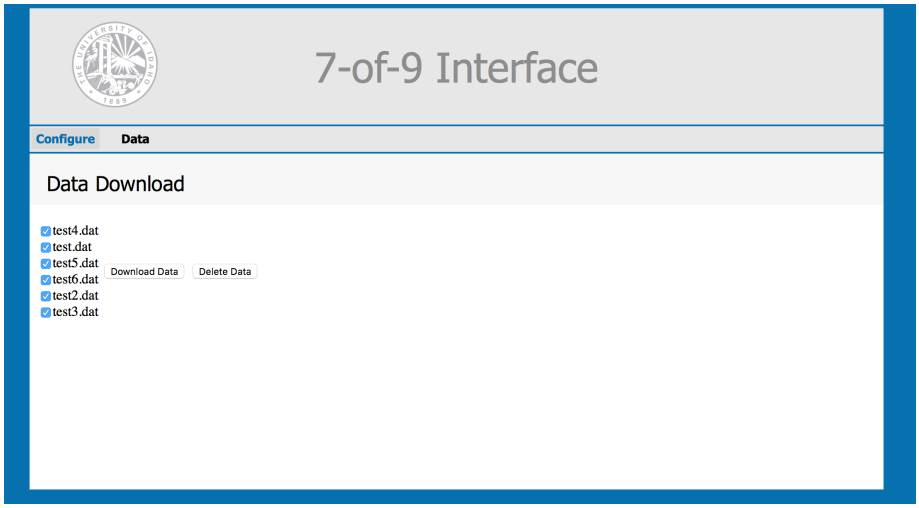


FIGURE 4.6: Data Download and Delete Page

CGI SCRIPTING — This system uses two distinct CGI scripts. One is used to download or delete prior data collection records and the other is for the user to input the sample sets. The download or delete script determines what files are on the SD Card then displays all files with the program specified filetype. The user can then select which files to delete or download using a series of checkboxes next to the file name. Files are then downloaded into a single zip file using a standard HTTP

file download protocol. Deleting files gives the user feedback as to which files were deleted and the page is refreshed to show the files remaining.

The other script validates the user input through a script which decodes what the user input and whether it meets the set criteria. If the supplied commands or sampling sets are not valid, the page will refresh and the user will be able to enter the information again. If the request is valid, the information is saved and the webserver will exit and the program will heed to the commands and data collection the user specified.

Command and Sampling Structure — A command structure is developed such that the user can specify the names of the files to be written, which data sets to write to those files, and many other specifications to suit the need for the application. Each command is given by specifying where in the program flow the command should be executed followed by the command and the commands parameters, if applicable. The commands included with this acquisition system are 'NF', 'WAIT', 'WAIT232', 'FM', 'TO', and 'SE'. The functionality of each of these commands is as follows:

1. NF: Create a new file followed by the name of the file.
2. WAIT: Wait for a number of seconds given by the number following the command. Continue sampling as normal after the time has elapsed.
3. WAIT232: Wait for an external RS232 command before continuing.
4. FM: Format the SD Card data storage device.
5. TO: Timeout after a number of minutes given by the number following the command. This causes all sampling to stop and system to restart after the time has elapsed.
6. SE: Securely erase the memory by filling it up with random data then erasing it. The number of times to perform this cycle is given by the number following the command.

The first line is reserved for commands, but subsequent lines are for specifying sampling sets. A sample set consists of number of samples, sample rate, and gain. Each sampling set line must contain a series of sample sets defined by the user. If the first line after the command line is utilized, but none of the other lines are used, it is assumed that the sample set information applies to all six channels, as shown in Figure 4.7. If the first line after the command line is utilized, but the next line has a new line, but nothing added, it is assumed the sample set information applies to the first three channels, as shown in Figure 4.8. If the first line after the command line is blank, but the line after that is utilized, it is assumed that the sample set information applies to the last three channels, as shown in Figure 4.9. Any other combination of usage of the sample sets applies to the channel corresponding to the line the sample sets were entered, an example is shown in Figure 4.9.

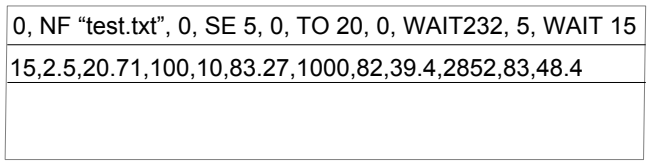


FIGURE 4.7: First Sample Line Populated - Sample on All Six Channels

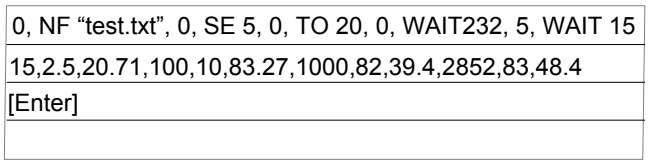


FIGURE 4.8: First Sample Line Populated with Next Line Unpopulated - Sample on First Three Channels

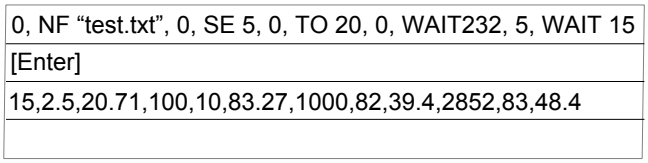


FIGURE 4.9: First Sample Line Unpopulated with Next Line Populated - Sample on Last Three Channels

| 0, NF “test.txt”, 0, SE 5, 0, TO 20, 0, WAIT232, 5, WAIT 15 |
| --- |
| [Enter] |
| [Enter] |
| 15,2.5,20.71,100,10,83.27,1000,82,39.4,2852,83,48.4 |

FIGURE 4.10: Third Sample Line Populated - Sample on Channel Three Only

CHAPTER 5

# Test Results and Noise Measurement[2]

## 5.1 INTRODUCTION

The preamplifier and the electrodes are characterized in terms of their respective noise. This noise defines where a signal may be detected and how well the components are working. In addition, a signal to noise ratio can show how well a signal is collected in comparison to its noise floor. With these two parameters, various components can be compared to determine the superior component or combination of components. The data acquisition system becomes another important factor to decreasing the noise floor and storing analog data. This chapter steps through the various stages of testing between the preamplifier, the data acquisition system, and the electrode ball probes.

## 5.2 DATA ACQUISITION SYSTEM

The data acquisition system is tested in parts to ensure proper functionality. Initially, a direct SPI link between the Intel Edison and the ADC was tested, but long delays between SPI commands rendered it inoperable. The need for a microcontroller interface surfaced to increase timing accuracy and eliminate delays between SPI messages. $I^2C$ was chosen as the communication protocol between the microcontroller and the Edison. The $I^2C$ connection between the Atmel and the Intel Edison requires level shifting to accommodate their respective voltage levels. This level shifting is known to cause data corruption on the Edison when data is being read. As such, all other system components are tested, but the communication between the microcontroller and the Edison is in need of adjustment. Upon further investigation, the Intel Edison was found to be the cause of the data corruption due to a relatively high voltage level corresponding to a logic one instead of a logic zero as intended [25].

[2]Portions of this chapter are adapted from "Methodology for Electric Potential Sensor Noise Measurements in Salt Water", published in: OCEANS 2016 - MTS/IEEE [24].

### 5.2.1 *Hardware*

The hardware connection is tested to be correct between the ADC and the Atmel as values can be read. The user-end wireless connection is working as expected on the Intel Edison. Additionally, if passing a few bytes of data at a time, parameters can be read from the Atmel over $I^2C$.

### 5.2.2 *Software*

Software can be tested in sections and called by overarching software. The shell script calls the webserver which then exits and the Python script takes over, upon valid user input, to execute the user commands. Commands are executed by system calls from the Python program, using open source software when possible to simplify the program and further improve reliability. Once the Python program is complete, the system is restarted using a system call.

Webserver and CGI scripts — The webserver is tested to boot up upon startup and host the webpage for user input. Once user input is received, the webserver quits hosting, as expected, and saves the user input to volatile memory. Python code waits for the user input to be saved then begins executing user instructions. Additionally, files can be stored on the SD card and retrieved in the user specified list of files and downloaded as a zip or deleted.

User Input Validation — User input validation scripts have been tested with a number of combinations including test cases expected to fail.

SD Card Data Retrieval and Deletion — The SD card read/write speed is found to be in excess of 23 $MB/s$. Additionally, with correct permission settings, the CGI scripts are able to successfully read and write data on the SD card.

## 5.3 NOISE MEASUREMENT PROCEDURE

The procedure developed herein ensures consistency between datasets. After consistency is achieved, modifications can be made and retesting completed to ensure improvement and aid in the engineering process. First, a consistent process to make similar measurements between datasets is developed, then parameters are tightly controlled, then data is compared to determine the effects of changes on the system. Changes may be necessary, but these may be made as long as dataset comparisons are between identically processed datasets. This standard decreases the likelihood that comparisons incur differing external interferences.

To determine the sources of noise, datasets from each sequential system component must be collected to be able to understand the entire system. The first step is to measure the noise of the data acquisition system itself. In doing this, a baseline noise measurement is made to where the lowest possible detection can be made. Second is to add in the next component and collect another set of data. This is repeated until the last system component is characterized, obtaining the overall system noise performance.

Systems can be characterized by removing the noise associated through previous systems using Equation 5.1 where sys1 and sys2 are connected as shown in Figure 5.1. The variable $Noise_{sys2_{Output}}$ is the noise measured at the output of the system, the gain is accounted for with the variable $Gain_{sys1}$, and the variables $Noise_{sys1}$ and $Noise_{sys2}$ are the self-noise of those respective systems. For this testing, the amplifier is characterized as $Noise_{sys1}$ and the NI 9239 is characterized as $Noise_{sys2}$. Subsequent systems are calculated in the same manner. This is used to calculate the noise of a single component when the noise is known for every other connected subsystem [26]. Additionally, noise is calculated using two methods. One method is calculation through the time domain signal and the other through the frequency domain signal. The frequency domain calculation is calculated using Equation 5.2 while the time domain calculation is calculated using Equation 5.3. Both results, if the frequency spectrum is calculated correctly, should be close to each other. The variable $\Delta f$ is the frequency change of frequency from one point of the FFT to the next and $V$ is the

resultant power spectral density (PSD). The variable $v$ is the time series voltage level and $l_v$ is the number of voltage level points [27].

$$Noise_{sys2_{Output}} = \sqrt{Gain_{sys1}^2 \times (Noise_{Input}^2) + Noise_{sys1}^2 + Noise_{sys2}^2} \tag{5.1}$$

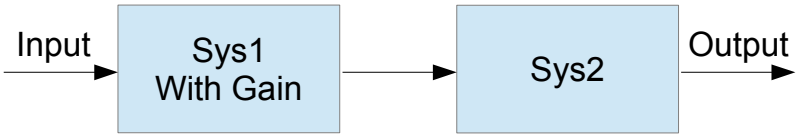


FIGURE 5.1: System Connection

$$Noise = \Delta f \times \sum V \tag{5.2}$$

$$Noise = \frac{\sum v^2}{l_v} \tag{5.3}$$

Care must be taken to ensure reputable noise measurements by creating a noise free environment. This includes the usage of a Faraday cage, shielding equipment, usage of shielded cables, and usage of ferrite cores. If this is done correctly, individual components, anywhere in the system, can be compared directly through the datasets. Additionally, it is advised to collect long periods of data at a sampling rate of at least two times the highest frequency, but preferably higher. The long period of data allows for picking and choosing time samples during post processing to obtain a high quality frequency spectrum.

The electrodes should be placed in the center of the tank to ensure the largest amount of external noise filtering from the water itself. The larger the tank, the better the noise filtering. A pump should be used to stir the tank prior to taking a measurement to ensure salt is equally distributed, but given roughly two hours to settle or the first few hours of data can be ignored in post processing. After adequately mixed, the salt water should be measured for salinity, in at least three different positions, to ensure consistent salinity between datasets.

## 5.4 MEASUREMENT METHODS

Water acts as a lowpass filter and shielding for RF, blocking frequencies above 10Hz [13]. The conductive nature of the seawater helps the ocean act as a low pass filter where noise is minuscule in deep water and strongly attenuated above a fraction of a Hertz in shallow water [28]. In addition, noise measurements have been found to be well below 1 $\mu V/m$ at frequencies above 1 $Hz$ [13]. Furthermore, attenuation of electromagnetic frequencies is shown in Figure 5.2 where attenuation is found to be approximately 1 $dB/m$ at 1 $kHz$ and 0.3 $dB/m$ at 300 $Hz$ with a linear rate. Therefore, the noise floor due to only the sensor probe, as designed in section 2.2.2, is expected to be higher than the noise floor of the ocean, meaning that the only signals expected to be detected are the man-made signals of interest. This also shows that any harmonics from frequencies above the intended frequency spectrum, though unlikely due to the low-pass nature of the ocean, must be from man-made signals. RF shielding is added to the laboratory equipment and measurement devices, as applicable, to reduce the likelihood of RF noise.

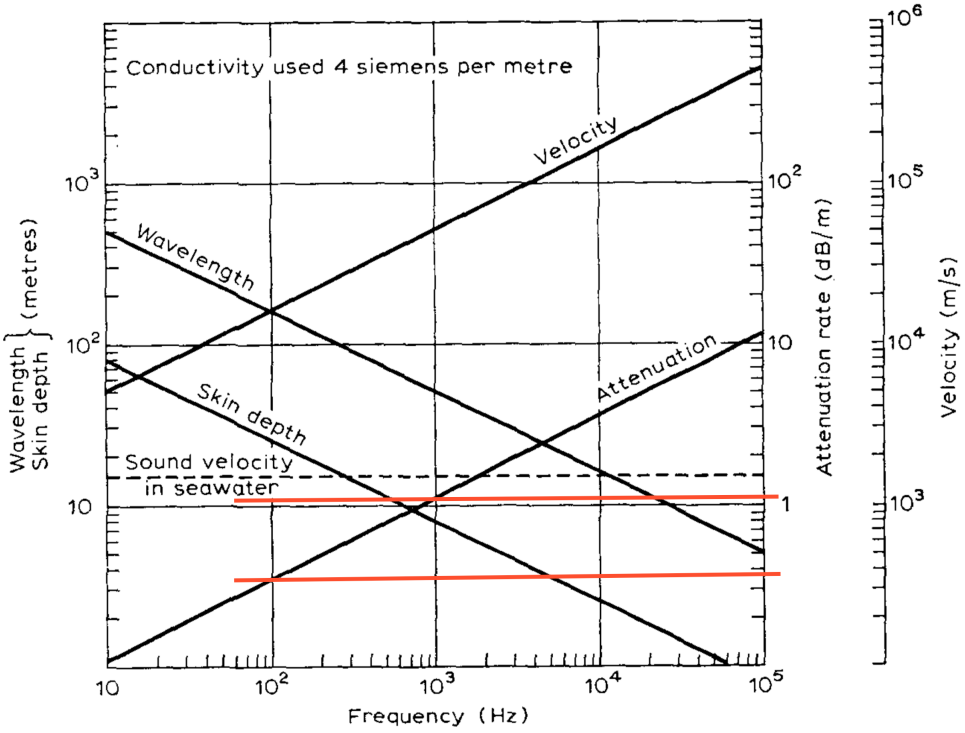


FIGURE 5.2: Electromagnetic Attenuation in the Ocean [2]

Testing is completed in the saltwater tank pictured in Figure 5.3. Batteries used for the tests consist of two Nickel-Metal Hydride batteries with 3.8AHr capacity at 7.2V. A fully charged battery measures around 7.8V and all testing is completed with batteries remaining over 7.5V. Measurement of the batteries is done both before initiating the test and after completion of the test. Furthermore, saltwater is measured with an Extech EC170 salinity meter at between 35.8 and 36.2 parts per thousand. Salinity measurements are completed prior to initiating each test, but two minutes after stirring the tank. The tank is stirred with a pump for greater than two minutes to ensure salt is equally distributed. The sensor probe is oriented in the same direction and placed at the same height each time to ensure consistency for correlating one test to another. In addition, if metal plates are added to induce an electric field, they are oriented in the same direction and same height each time for consistency.

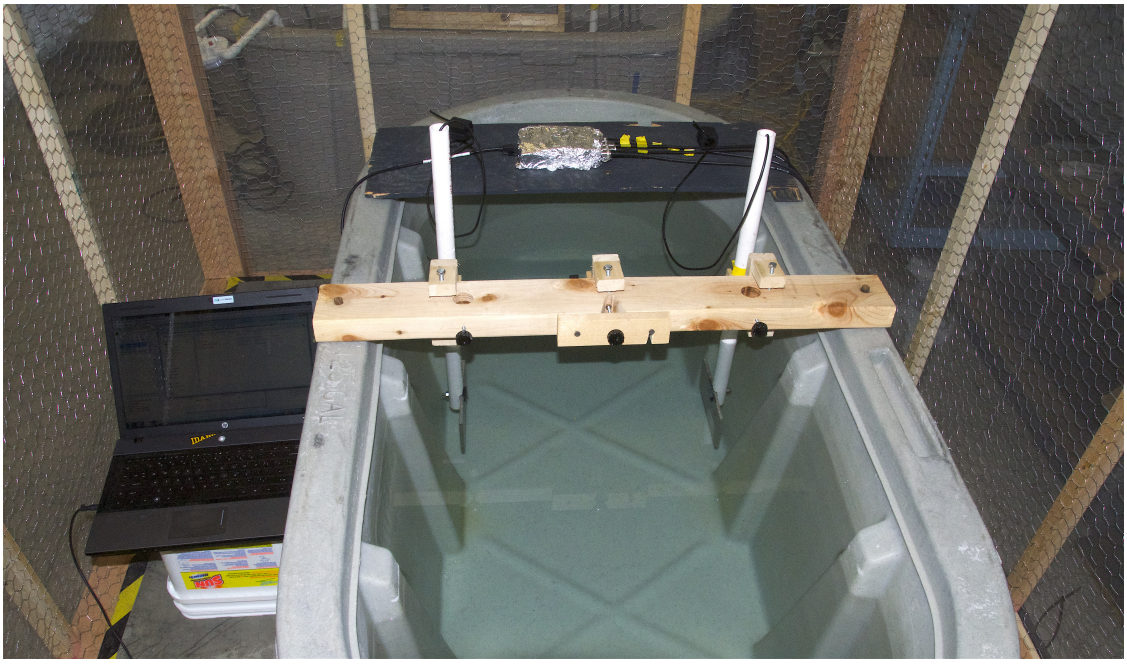

FIGURE 5.3: Salt Water Tank and Test Equipment (NIDAQ and Metal Plates)

Measurements of the electric field sensors are completed with a National Instruments (NI) 9239 Data Acquisition System. Noise floor measurements consisting of 30 hours of data collection of the NI 9239 itself with shorted leads are taken. This device uses a 24-bit ADC capable of 50 $kSPS$. Data collection uses a sample rate of 5 $kSPS$, due to the highest expected frequency for detection being 1 $kHz$. Radio Frequency

(RF) shielding is added where possible to reduce external noises. This RF shielding consists primarily of aluminum foil with metal enclosures where appropriate in addition to the Faraday cage shown in Figure 5.4. In regards to RF noise, the 3-inch probe is surrounded by water while the amplifier for the 1.5-inch probe is out of the water where RF noise is more of a concern. Due to this uncontrolled variable and higher expected noise level, the 1.5-inch probe data is neglected in these comparisons. The output of the amplifier is connected into the NI 9239 which has a digital lowpass filter, with 100 $dB$ rejection, at 0.453 $f_s$ where $f_s$ is the sampling frequency, $f_s = 5\ k$ in this testing. For the 1.5-inch probe in particular, the signal input to the amplifier contains the RF noise amplified by 48 $dB$. The amplified signal is then input into the NI 9239 and high frequency components are filtered. Since the noise is added prior to being amplified, the filtered signal still contains some of the aliased components. Further details are supplied in Appendix E.

FIGURE 5.4: Faraday Cage Containing Salt Water Tank and Test Equipment

## 5.5 POST PROCESSING FREQUENCY ANALYSIS

A fast Fourier transform (FFT) is used to convert from the time domain to the frequency domain. This displays the noise performance or signals of interest broken into their respective frequency components, allowing data to be visually seen and easily calculated. Processing is completed with MATLAB using the scripts in Appendix C. The script for Amplitude Spectral Density (ASD) has three options for windowing. Normally the Kaiser Bessel window is used due to its good overall performance when compared to other windows [29].

## 5.6 NOISE CHARACTERISTICS

These characteristics are measured in compliance with the procedure set in section 5.4. Noise is measured in the units of volts RMS ($V_{RMS}$). A calculation is necessary to take into account the electrode separation and the gain. These values are expected to be valid for any range of diameter or gain of amplifier. For this reason, measurements are left in $V_{RMS}$, but also discussed in terms of $V_{RMS}/m$ when taken as sensor input-referred noise. The numbers given show an average over a 28 to 30 hour segment of time.

### 5.6.1 *NI 9239*

This test consists of test leads shorted at the end and connected to the NI 9239 to measure the self-noise of the system up to where components will be connected. Figure 5.5 shows the original time series of the NIDAQ data. Matlab's detrend function is used to fix the DC offset by finding a best fit line and affixing the line as the y-axis 'zero'. The detrended data is shown in Figure 5.6. The frequency spectrum for the detrended data is shown in Figure 5.7. Additionally, total noise measurements are completed and shown in Table 5.1. From this, the average total noise is found to be 29.608 $\mu V_{RMS} \approx 30\ \mu V_{RMS}$.

TABLE 5.1: NIDAQ Noise Measurement (After Detrending)

| Channel | Time Domain Noise | Frequency Domain Noise |
|---|---|---|
| 0 | 30.155 $\mu V_{RMS}$ | 30.119 $\mu V_{RMS}$ |
| 1 | 29.327 $\mu V_{RMS}$ | 29.342 $\mu V_{RMS}$ |
| 2 | 29.435 $\mu V_{RMS}$ | 29.424 $\mu V_{RMS}$ |
| 3 | 29.539 $\mu V_{RMS}$ | 29.519 $\mu V_{RMS}$ |
| Average | 29.614 $\mu V_{RMS}$ | 29.601 $\mu V_{RMS}$ |
| Total Average | 29.608 $\mu V_{RMS}$ | |

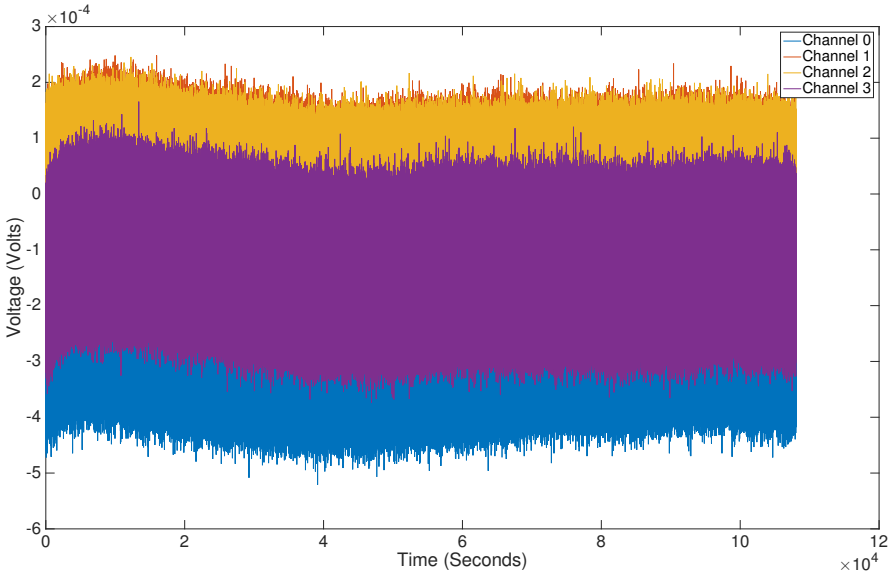


FIGURE 5.5: NIDAQ Time Series Data

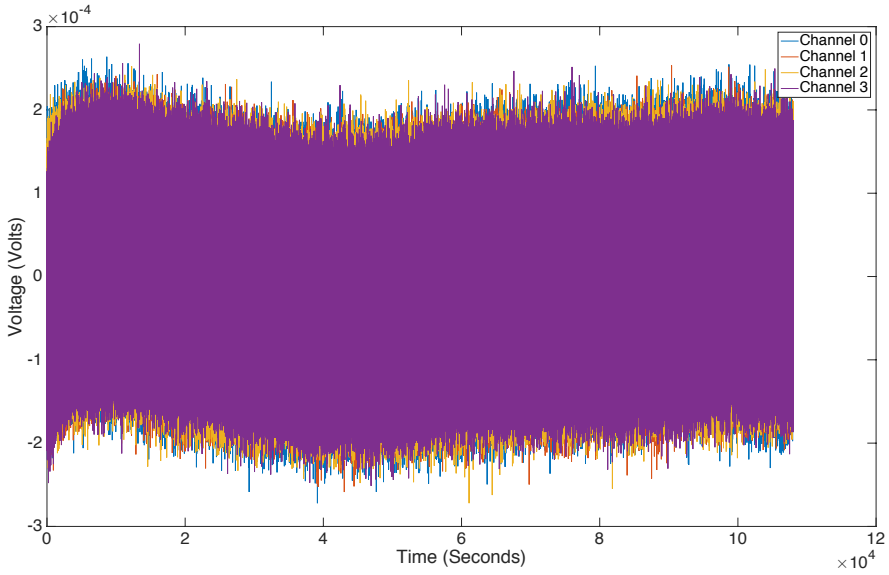


FIGURE 5.6: NIDAQ Time Series Data (Detrended)

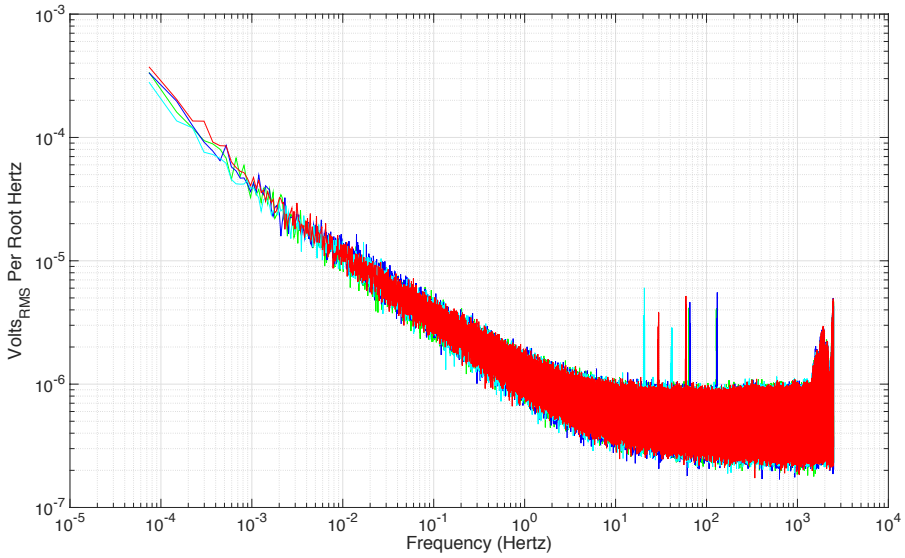


FIGURE 5.7: NIDAQ Frequency Spectrum Data

### 5.6.2 *INA129 vs INA333*

This test consists of comparing the INA129 with shorted inputs to the INA333 with shorted inputs. The INA129 is on a printed circuit board with three channels while the INA333 is in a breadboarded configuration with only two channels. Table 5.2 shows the noise measurement results. With the INA129, channel U3 is ignored in the

average row due to the difference between the other two channels. This is likely an issue due to external noise or a loose connection. Both devices are set with a gain of 250. The data shows the noise measurement close to the noise floor of the NIDAQ such that the noise is hidden by the noise floor of the measurement device. Figure 5.8 and Figure 5.9 show the time signals for the INA129 and INA333 respectively.

TABLE 5.2: INA129 vs INA333 Noise Measurement (After Detrending)

| Channel | Time | Frequency | Time | Frequency |
|---|---|---|---|---|
| | INA129 | | INA333 | |
| U1 | 28.279 $\mu V_{RMS}$ | 28.375 $\mu V_{RMS}$ | 30.000 $\mu V_{RMS}$ | 29.982 $\mu V_{RMS}$ |
| U2 | 29.604 $\mu V_{RMS}$ | 29.475 $\mu V_{RMS}$ | 30.265 $\mu V_{RMS}$ | 30.256 $\mu V_{RMS}$ |
| U3 | 0.3212 $mV_{RMS}$ | 0.3292 $mV_{RMS}$ | – | – |
| Average | 28.942 $\mu V_{RMS}$ | 28.925 $\mu V_{RMS}$ | 30.133 $\mu V_{RMS}$ | 30.119 $\mu V_{RMS}$ |
| Total Average | 28.934 $\mu V_{RMS}$ | | 30.126 $\mu V_{RMS}$ | |

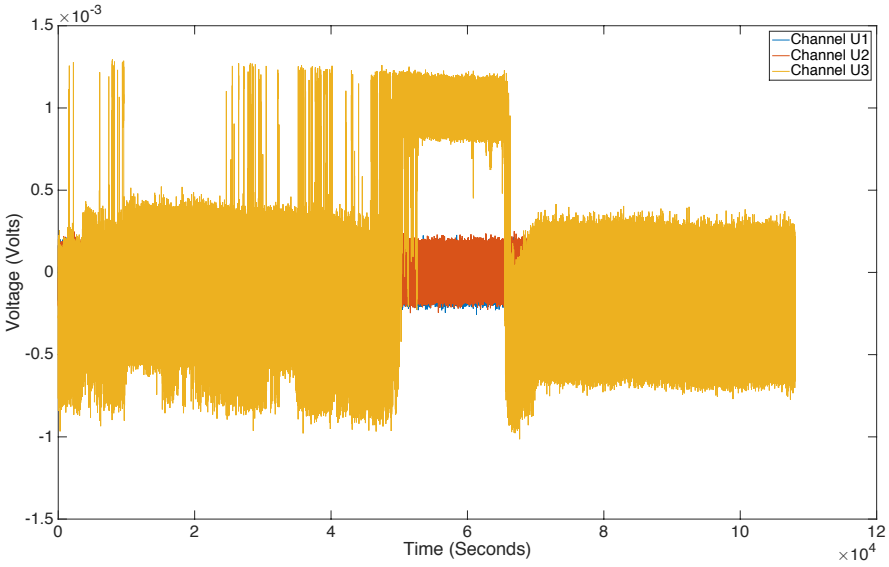


FIGURE 5.8: INA129 Time Series Data (Detrended)

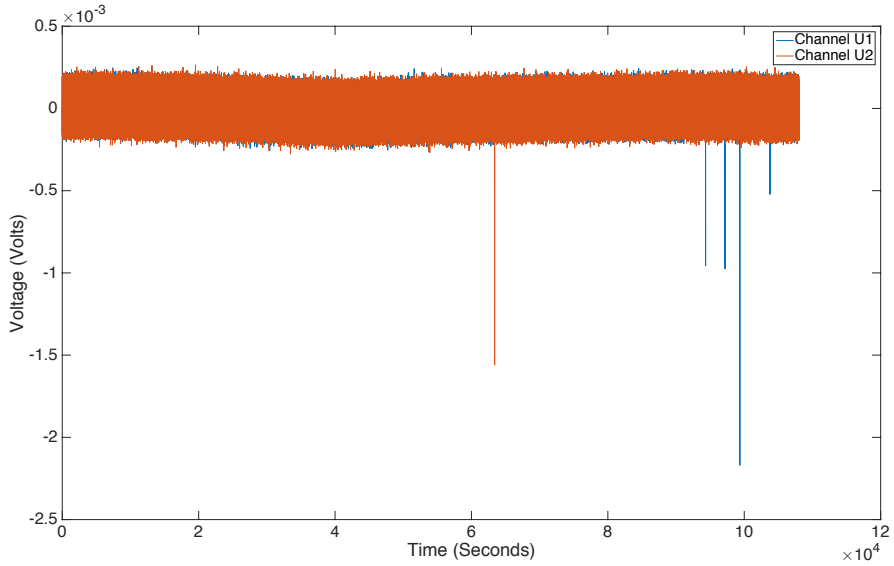


FIGURE 5.9: INA333 Time Series Data (Detrended)

### 5.6.3 *Electrode Settling Time*

The settling time can be seen in Figure 5.10 and Figure 5.11 where the 3-inch electrode ball probes are moved from air into water. This data leads to the advice to allow the electrodes to settle for at least 90 minutes before obtaining data due to the lack of reliable low frequency data before that time.

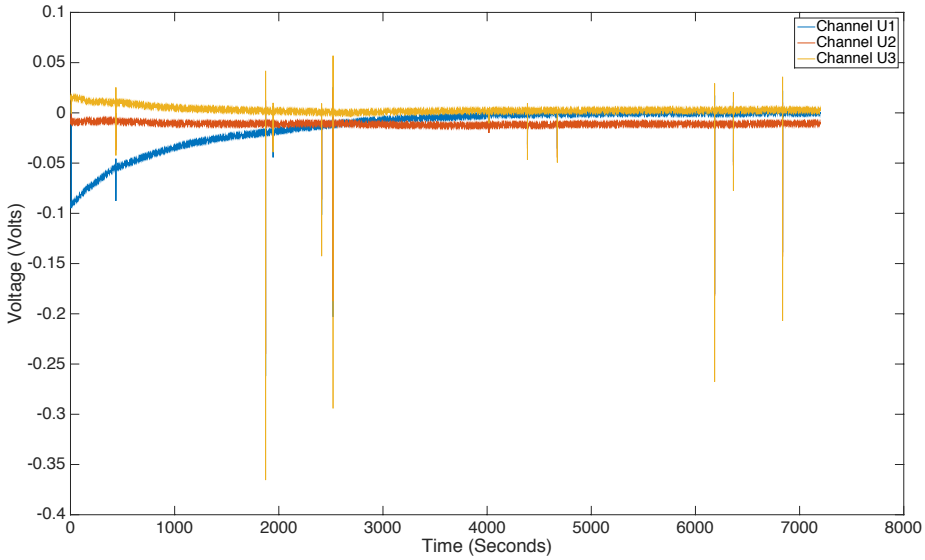


FIGURE 5.10: 3-inch Cylindrical Electrode Settling Time

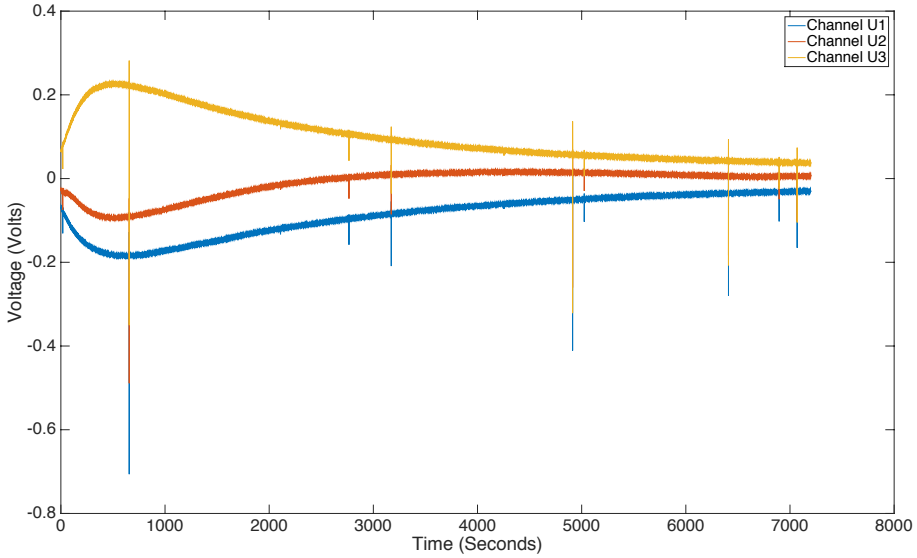


FIGURE 5.11: 3-inch Disc Electrode Settling Time

### 5.6.4 *3-inch Cylindrical Electrodes vs 3-inch Disc Electrodes*

With this comparison, two sets of data are taken. One with the 3-inch cylindrical electrode ball probe and one with the 3-inch disc electrode ball probe. Each of these sets of data are taken for 30 hours, with 28 hours shown herein to account for settling time. Both are oriented in the same direction, with the fill funnel facing the NIDAQ end of the tank and at the same height. Spikes are noticed in the time series, but are reduced with a range filtering function. Table 5.3 and Table 5.4 show the noise values between the two sets of data; one after detrending and the other with detrending and range filtering. The code for range filtering is given in Appendix C. It can be noticed that the range filtering has a small effect on the noise measurements. Figure 5.12 and Figure 5.16 show the detrended time series for cylindrical electrodes and disc electrodes respectively. Figure 5.14 and Figure 5.18 show the frequency spectrum for the corresponding detrended time series data. Figure 5.13 and Figure 5.17 show the same time series data, but range filtering is included in addition to detrending. Figure 5.15 and Figure 5.19 show the frequency spectrum for the corresponding detrended and range filtered time series data. Using Equation 5.1 from section 5.3, the noise measurement values 0.9329 $mV_{RMS} \approx 0.93\ mV_{RMS}$ and 3.7999 $mV_{RMS} \approx 3.8\ mV_{RMS}$, and the noise of the amplifier and NI 9239 of 30 $\mu V_{RMS}$

from section 5.6.1, the noise at the electrodes can be found. This noise is found as $\sqrt{\frac{(0.93\ mV_{RMS})^2-(30\ \mu V_{RMS})^2}{250^2}} = 3.72\ \mu V_{RMS}$ at the electrodes of the 3-inch cylindrical probe and $\sqrt{\frac{(3.8\ mV_{RMS})^2-(30\ \mu V_{RMS})^2}{250^2}} = 15.20\ \mu V_{RMS}$ at the electrodes of the 3-inch disc probe. Accounting for the separation distance, a $\frac{3.72\ \mu V_{RMS}}{3\times0.0254\times1.5\ m} = 31.08\ \mu V_{RMS}/m$ noise floor is found on the cylindrical ball probe and a $\frac{15.20\ \mu V_{RMS}}{3\times0.0254\times1.5\ m} = 126.99\ \mu V_{RMS}/m$ noise floor is found on the disc ball probe.

TABLE 5.3: Cylindrical vs Disc Noise Measurement (After Detrending)

| Channel | Time | Frequency | Time | Frequency |
|---|---|---|---|---|
| | 3-inch Cylindrical | | 3-inch Disc | |
| U1 | 0.8080 $mV_{RMS}$ | 0.7878 $mV_{RMS}$ | 2.6512 $mV_{RMS}$ | 2.3273 $mV_{RMS}$ |
| U2 | 1.5600 $mV_{RMS}$ | 1.5276 $mV_{RMS}$ | 4.8558 $mV_{RMS}$ | 4.3420 $mV_{RMS}$ |
| U3 | 0.4621 $mV_{RMS}$ | 0.4522 $mV_{RMS}$ | 4.6208 $mV_{RMS}$ | 4.0021 $mV_{RMS}$ |
| Average | 0.9434 $mV_{RMS}$ | 0.9225 $mV_{RMS}$ | 4.0426 $mV_{RMS}$ | 3.5571 $mV_{RMS}$ |
| Total Average | 0.9329 $mV_{RMS}$ | | 3.7999 $mV_{RMS}$ | |

TABLE 5.4: Cylindrical vs Disc Noise Measurement (After Detrending and Range Filtering)

| Channel | Time | Frequency | Time | Frequency |
|---|---|---|---|---|
| | 3-inch Cylindrical | | 3-inch Disc | |
| U1 | 0.8000 $mV_{RMS}$ | 0.7865 $mV_{RMS}$ | 2.6501 $mV_{RMS}$ | 2.3259 $mV_{RMS}$ |
| U2 | 1.5863 $mV_{RMS}$ | 1.5270 $mV_{RMS}$ | 4.6901 $mV_{RMS}$ | 4.1988 $mV_{RMS}$ |
| U3 | 0.4701 $mV_{RMS}$ | 0.4478 $mV_{RMS}$ | 4.5840 $mV_{RMS}$ | 3.9387 $mV_{RMS}$ |
| Average | 0.9521 $mV_{RMS}$ | 0.9204 $mV_{RMS}$ | 3.9747 $mV_{RMS}$ | 3.4878 $mV_{RMS}$ |
| Total Average | 0.9363 $mV_{RMS}$ | | 3.7313 $mV_{RMS}$ | |

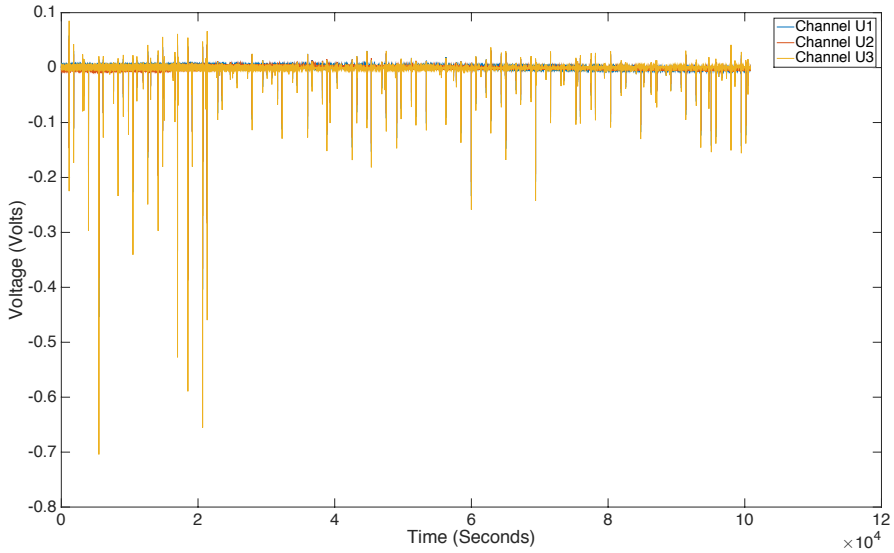


FIGURE 5.12: Cylindrical Electrode Time Series (After Detrending)

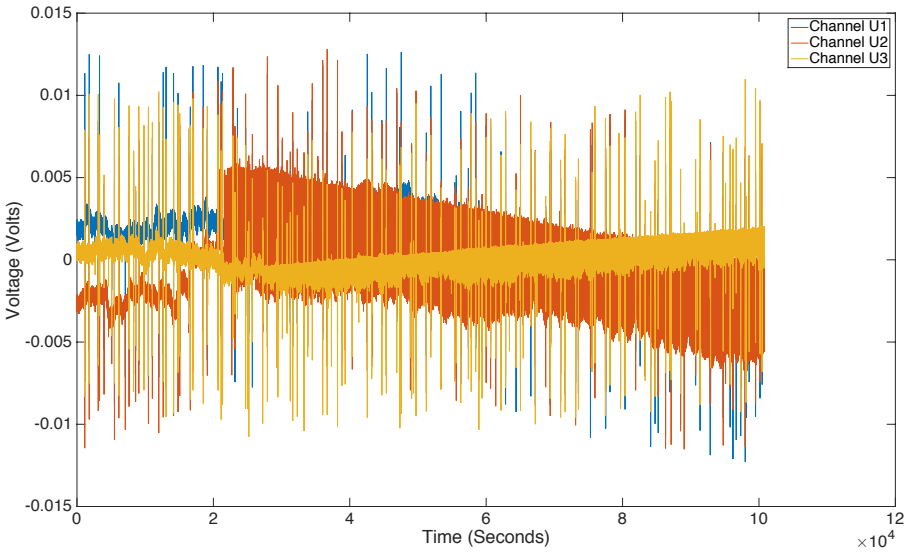


FIGURE 5.13: Cylindrical Electrode Time Series (After Detrending and Range Filtering)

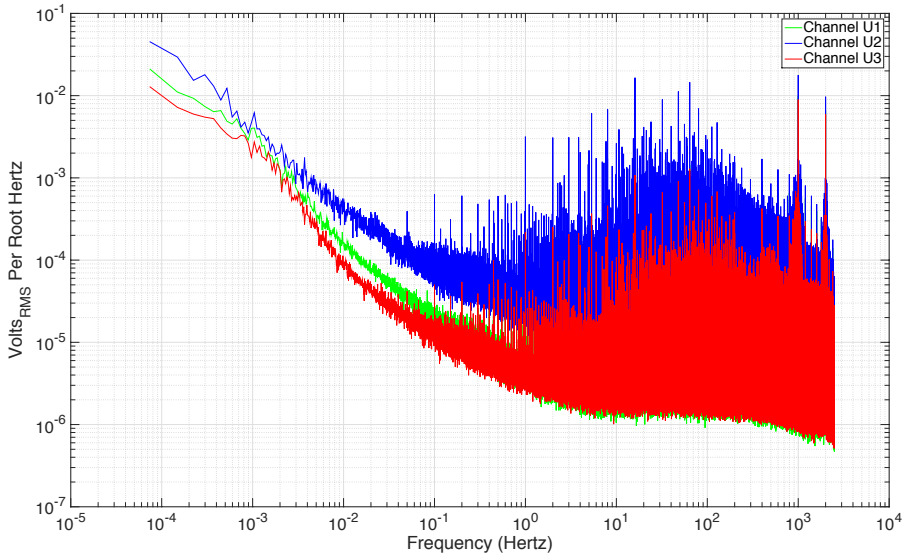


FIGURE 5.14: Cylindrical Electrode Frequency Spectrum (After Detrending)

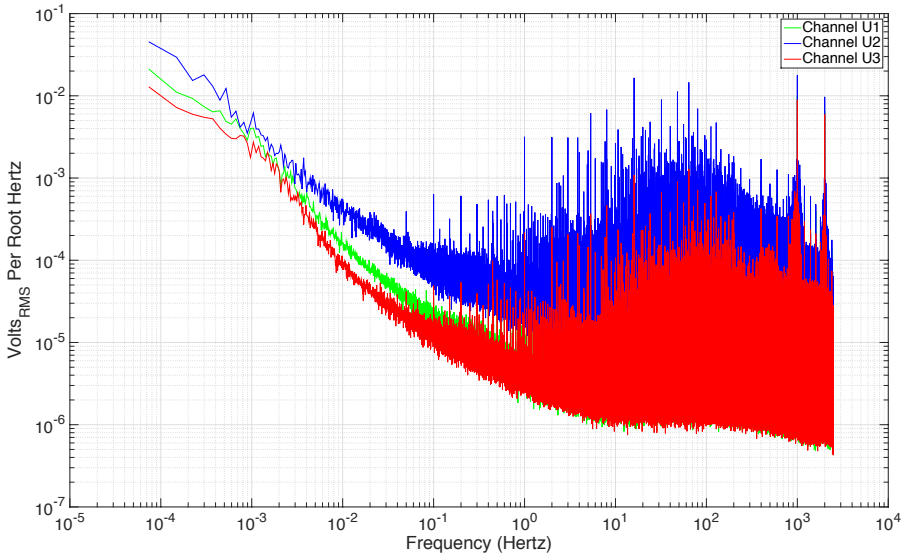


FIGURE 5.15: Cylindrical Electrode Frequency Spectrum (After Detrending and Range Filtering)

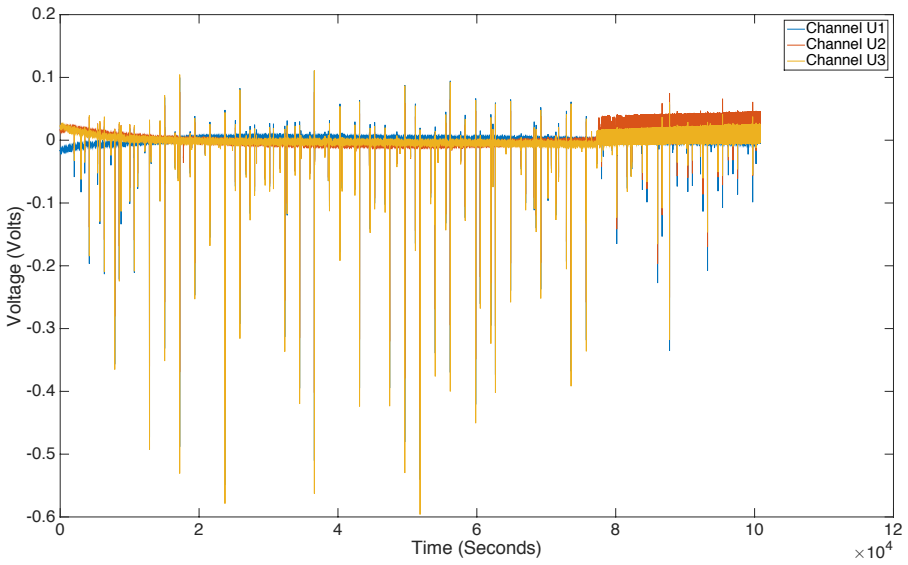


FIGURE 5.16: Disc Electrode Time Series (After Detrending)

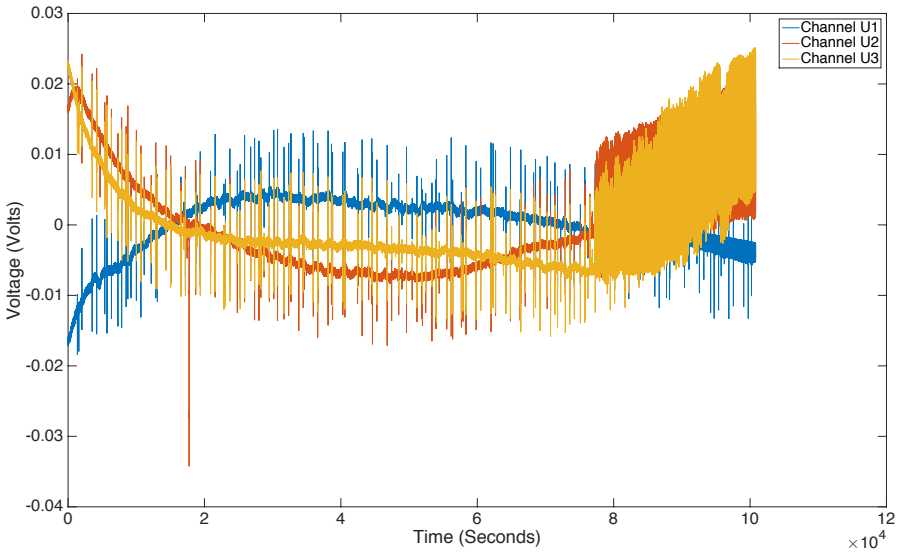


FIGURE 5.17: Disc Electrode Time Series (After Detrending and Range Filtering)

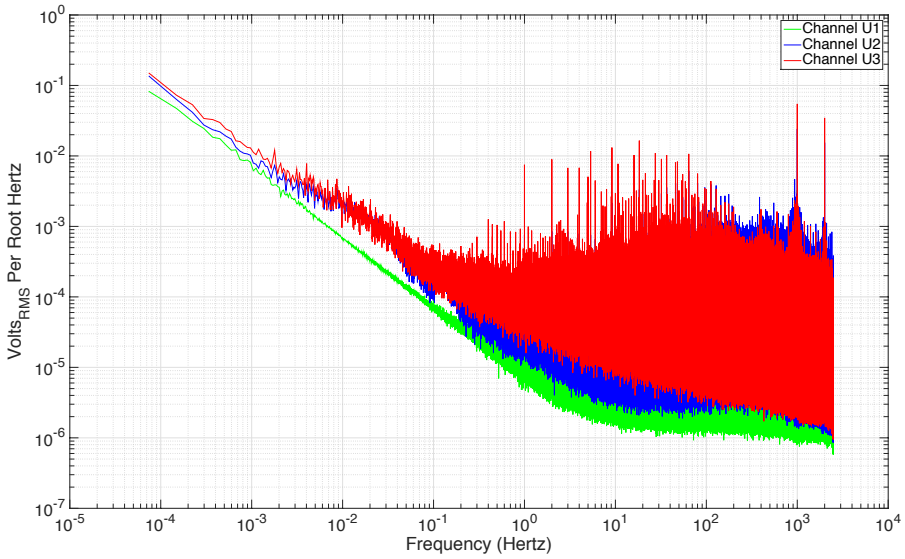


FIGURE 5.18: Disc Electrode Frequency Spectrum (After Detrending)

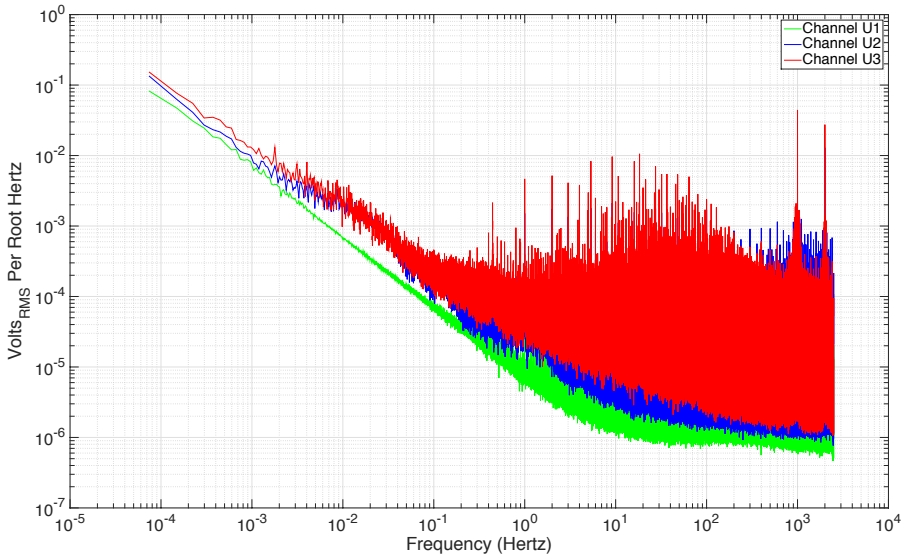


FIGURE 5.19: Disc Electrode Frequency Spectrum (After Detrending and Range Filtering)

### 5.6.5 *Effects of Agar on Electrode Ball Probe*

Agar is mixed with the salt water from the test tank and placed directly on top of the electrodes. Once cured, the ball probes are placed in the test tank and one is tested at a time. Testing is completed in the same manner, and same ball probes, as in section 5.6.4. It is important to mix the agar with the water from the area

the electrodes will be used in as to ensure the correct concentration of salt to water. Table 5.5 shows the noise values for the corresponding cylindrical and disc electrode tests. Channel U3 of the disc electrode is ignored in the average calculations due to the high noise level. This noise may have been induced by the agar since it can be seen in section 5.6.4 that, for the same electrode ball probe, the noise value is close to the other two channels. Figure 5.20 and Figure 5.22 show the time series data for the cylindrical and disc electrodes respectively. Figure 5.21 and Figure 5.23 show the frequency spectrum for the cylindrical and disc electrodes respectively. Using Equation 5.1 from section 5.3, the noise measurement values 1.8154 $mV_{RMS} \approx 1.82\ mV_{RMS}$ and 1.1637 $mV_{RMS} \approx 1.16\ mV_{RMS}$, and the noise of the amplifier and NI 9239 of 30 $\mu V_{RMS}$ from section 5.6.1, the noise at the electrodes can be found. This noise is found as $\sqrt{\frac{(1.82\ mV_{RMS})^2-(30\ \mu V_{RMS})^2}{250^2}} = 7.28\ \mu V_{RMS}$ at the electrodes of the 3-inch cylindrical probe and $\sqrt{\frac{(1.16\ mV_{RMS})^2-(30\ \mu V_{RMS})^2}{250^2}} = 4.64\ \mu V_{RMS}$ at the electrodes of the 3-inch disc probe. Accounting for the separation distance, a $\frac{7.28\ \mu V_{RMS}}{3\times 0.0254\times 1.5\ m} = 60.82\ \mu V_{RMS}/m$ noise floor is found on the cylindrical ball probe and a $\frac{4.64\ \mu V_{RMS}}{3\times 0.0254\times 1.5\ m} = 38.77\ \mu V_{RMS}/m$ noise floor is found on the disc ball probe.

TABLE 5.5: Cylindrical vs Disc Agar Noise Measurement (After Detrending)

| Channel | Time | Frequency | Time | Frequency |
|---|---|---|---|---|
| | 3-inch Cylindrical | | 3-inch Disc | |
| U1 | 2.2066 $mV_{RMS}$ | 2.1782 $mV_{RMS}$ | 1.5679 $mV_{RMS}$ | 1.5692 $mV_{RMS}$ |
| U2 | 2.3713 $mV_{RMS}$ | 2.3581 $mV_{RMS}$ | 0.7871 $mV_{RMS}$ | 0.7307 $mV_{RMS}$ |
| U3 | 0.9181 $mV_{RMS}$ | 0.8600 $mV_{RMS}$ | 7.8067 $mV_{RMS}$ | 7.8072 $mV_{RMS}$ |
| Average | 1.8320 $mV_{RMS}$ | 1.7988 $mV_{RMS}$ | 1.1775 $mV_{RMS}$ | 1.1500 $mV_{RMS}$ |
| Total Average | 1.8154 $mV_{RMS}$ | | 1.1637 $mV_{RMS}$ | |

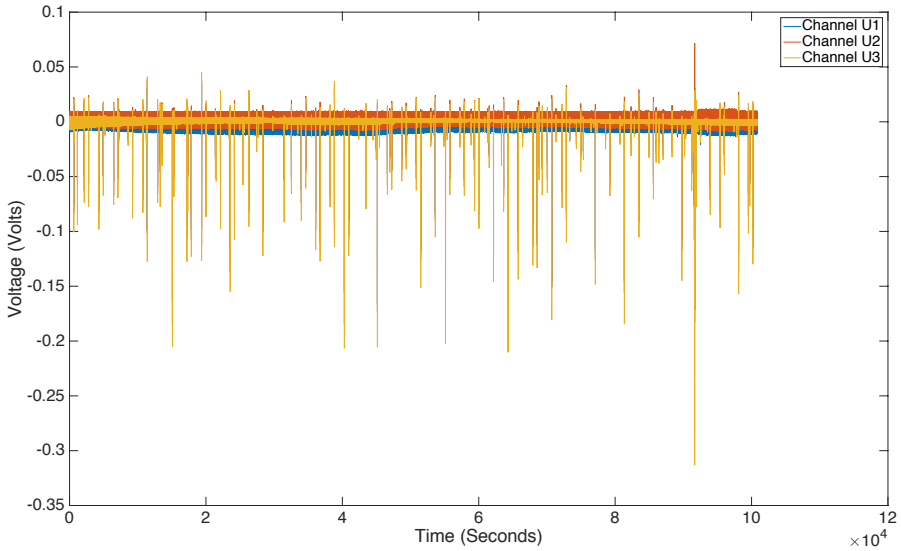


FIGURE 5.20: Cylindrical Electrode with Agar Time Series

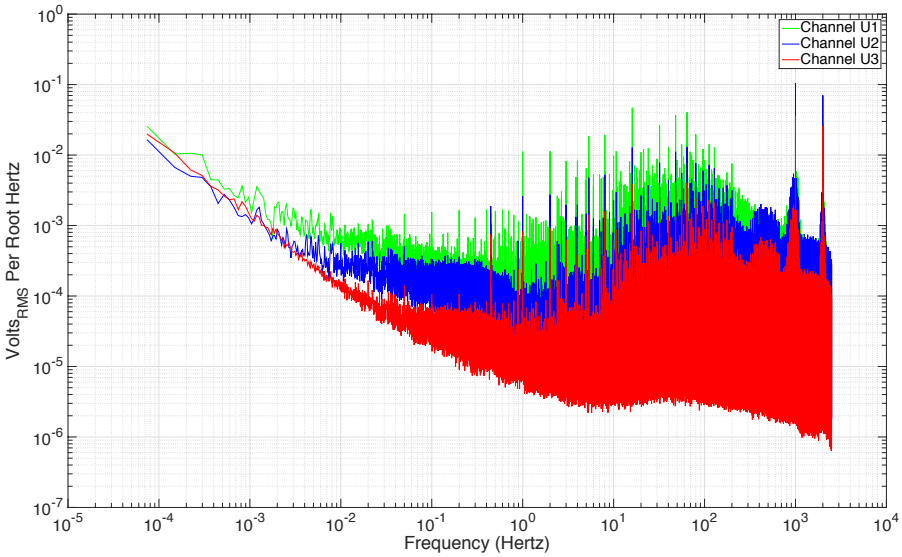


FIGURE 5.21: Cylindrical Electrode with Agar Frequency Spectrum

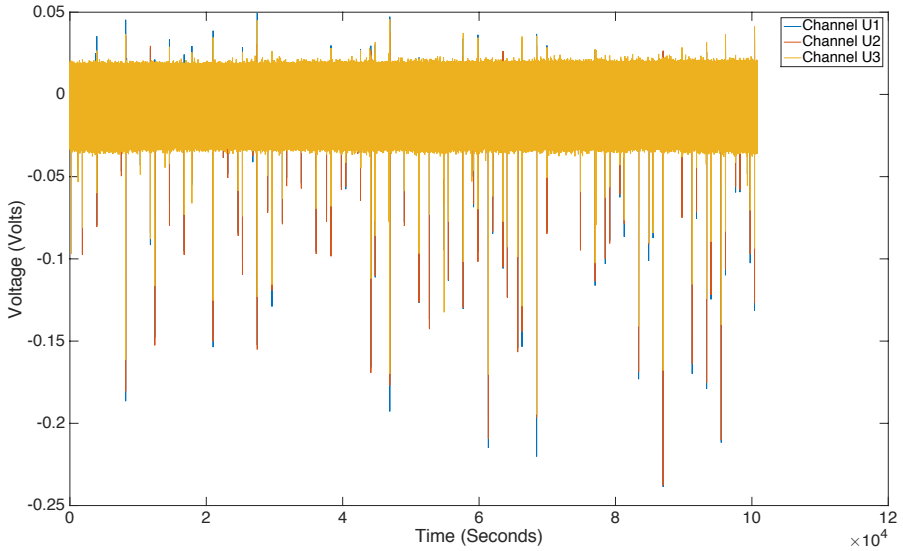


FIGURE 5.22: Disc Electrode with Agar Time Series

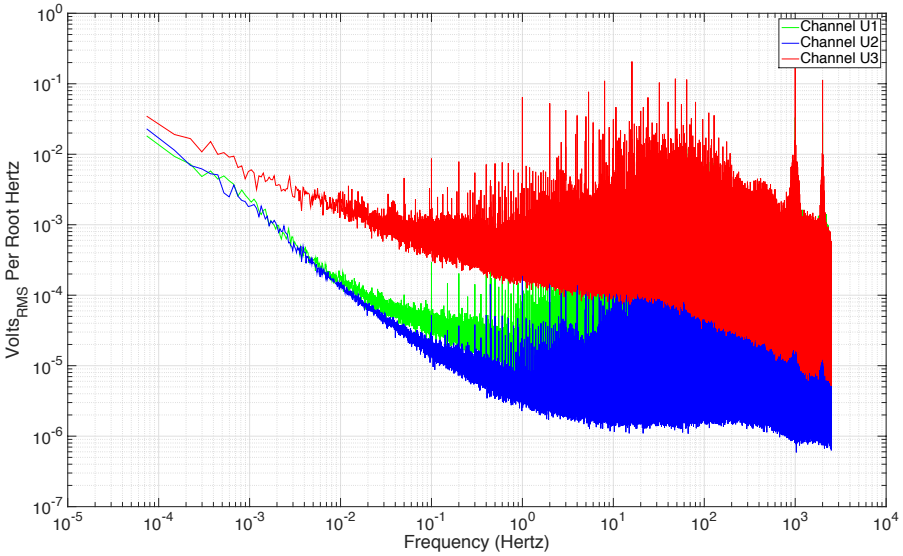


FIGURE 5.23: Disc Electrode with Agar Frequency Spectrum

## 5.7 CHARACTERISTICS WITH A SIGNAL

Both the 3-inch cylindrical ball probe with agar and the 3-inch disc ball probe with agar are tested. The input signal consists of a 2 $mA$, 0.7 $Hz$ sine wave generated from a Keithley 6221 current source. This signal can be seen on the time series in Figure 5.24 for the cylindrical ball probe and Figure 5.25 for the disc ball probe. The frequency

spectrum is calculated and shown in Figure 5.26 for the cylindrical ball probe and Figure 5.27 for the disc ball probe. It can be seen from the frequency spectrum that both ball probe configurations amplify the signal to approximately the same amount, but the disc ball probe has a more linear frequency response.

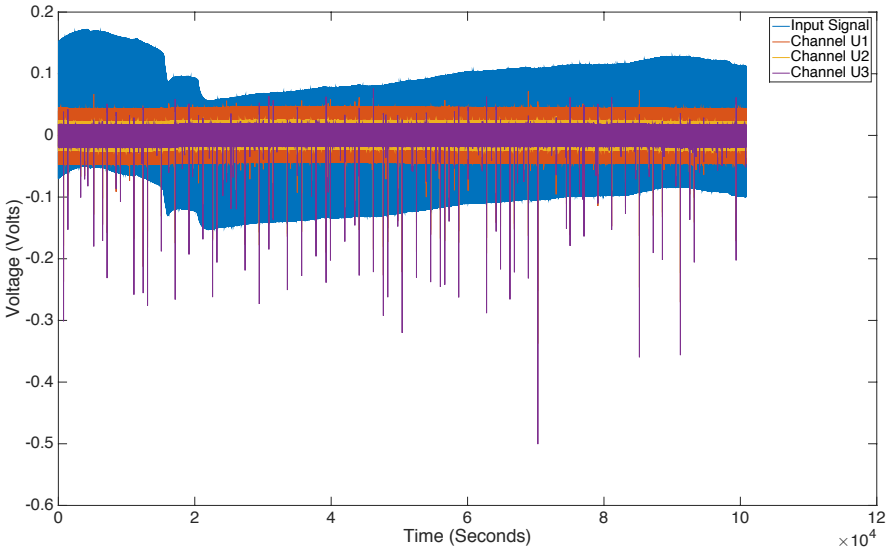


FIGURE 5.24: Cylindrical Electrode Time Series

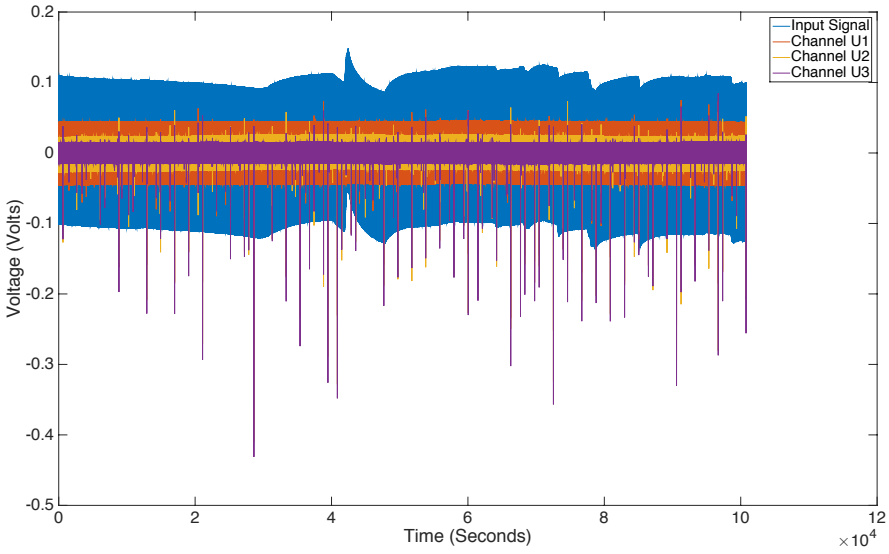


FIGURE 5.25: Disc Electrode Time Series

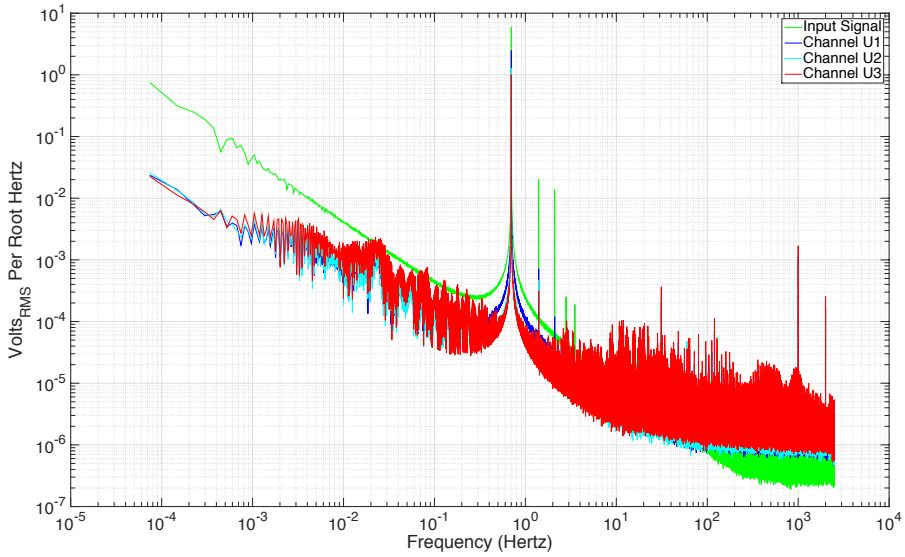


FIGURE 5.26: Cylindrical Electrode Frequency Spectrum

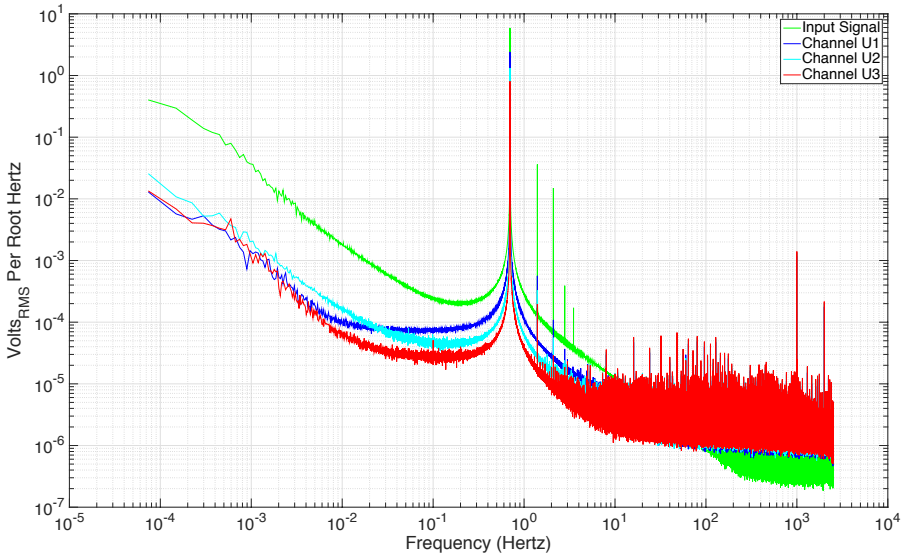


FIGURE 5.27: Disc Electrode Frequency Spectrum

chapter 6

# Conclusions

Chapter 2 discusses the sensors used to sense electric fields in seawater and proposes the use of a ball probe sensor design with silver-silver chloride electrodes. The 3-inch disc sensor ball probe is the hardware recommended due to the larger electrodes and separation distance.

Chapter 3 discusses the two major types of amplifiers used for obtaining high input impedance, differential input, high gain, and low-noise at low-frequencies. Two amplifiers are developed and recommended for use. The INA129 amplifier board is recommended for higher frequency measurements while the INA333 amplifier board is recommended for ultra-low frequency measurements. The frequency to switch amplifiers is expected to be less than 0.1 $Hz$, but testing with electrode ball probes will be necessary to determine this point.

Chapter 4 discusses the modernized data acquisition hardware and proposes the use of an Intel Edison in combination with Atmel microcontroller and TI 32-bit ADC due to the physical size, low-power usage, and modular design. Additionally, software is shown to facilitate the user interface, all necessary connections to subsystems, and allow flexibility for changes.

Chapter 5 discusses the noise measurements on the ball probes of Chapter 2 and the amplifiers in Chapter 3. In addition, the results from the digital user input are discussed, the program flow is validated. The noise of the 3-inch cylindrical ball probe is found to be approximately 3.72 $\mu V_{RMS}$ without agar and 7.28 $\mu V_{RMS}$ with agar. While the noise of the 3-inch disc ball probe is found to be approximately 15.20 $\mu V_{RMS}$ without agar and 4.64 $\mu V_{RMS}$ with agar. A larger surface area is obtained with the 12 $mm$ diameter disc electrodes, but further testing is necessary to determine the advantages.

CHAPTER 7

# Future Work

## 7.1 ELECTRIC FIELD SENSORS

### 7.1.1 *Usage of Larger Electrodes*

The likelihood of the Ag/AgCl electrodes being affected by noise in the lab is much higher than in the open ocean. This is due to the proximity of noise sources and relatively shallow depth of water. In addition, the small physical size of the electrodes creates a lower signal-to-noise ratio than larger electrodes would. "The potentials of smaller electrodes were disturbed to a relatively greater extent because of the smaller surface area in contact with solution. This observation leads to the recommendation that very small electrodes be shielded in a Faraday cage during measurement to reduce the noise influence when high precision is required." [30] Increasing the physical dimensions of the electrodes should reduce the impact of noise on sensor data.

### 7.1.2 *Usage of Carbon Fiber Electrodes*

Carbon fiber electrodes are relatively new to the seawater electric field sensing. These electrodes have been shown to work down to approximately 1 $mHz$ which may be adequate to produce desired results in oceanic measurements. However, these electrodes are capacitive and work optimally at higher frequencies. The capacitive nature is also a benefit since they may not need to come into direct contact with the seawater.

## 7.2 PREAMPLIFIER

Implementation of an imbedded INA333 amplifier in a 3-inch disc ball probe can be compared to the INA129 3-inch disc ball probe to determine improvements at ultra-low frequencies.

## 7.3 DATA ACQUISITION SYSTEM

### 7.3.1 *Hardware*

Using the 3-inch ball probe with an integrated amplifier in lieu of the 1.5-inch ball probe signal conditioning circuitry will not be necessary for half of the inputs to the DAQ. Additionally, by using a 5 $V$ magnetometer, the other half of the signal conditioning circuitry will not be necessary. This redesign will cut the physical board size by around 40% resulting in an even smaller footprint. The instrumentation amplifiers in the ball probes may act as signal conditioning for the ADC by utilizing the reference voltage on the ADC as the reference of the ball probe. Additionally, errors are noted in the $I^2C$ line in the conversion of large data between 1.8 $V$ and 3.3 $V$. These errors can be avoided by utilizing a USB link between the two devices which may also further modularize the device by allowing connection to a computer in lieu of an Intel Edison.

### 7.3.2 *Software Delays*

Software delays exist where a parasitic delay occurs between each sample set. Observing from the analog circuitry up to the digital data storage, no delays are seen between the analog circuitry and the ADC. Delays are seen between the ADC and the Atmel, however they are inconsequential due to the fact that the ADC rate is set higher than the desired sample rate and the timer in the Atmel is continually counting. The link between the Atmel and the Edison does add delay, but this delay is only seen when transitioning to another sample set. At that point, it takes a minimum of 13 bytes to set up a sample set due to the transmission of the channel information, rate information, number of samples, and associated addressing. With a data rate of 400 $kbps$ this results in a best case delay of approximately $\frac{13\times 8}{400{,}000} = 0.26\ ms$ per sample set. This may be addressed by buffering the next sample set while the current one is being performed. However, these delays are acceptable due to the navigation system accuracy of around 0.83 *meters* in simulation [31]. With the AUV maximum speed of approximately 1 meter per second, a total delay of 800 $ms$ will be small in regards to corresponding the measurement with where it was taken.

### 7.3.3 *Further Usage of RF Shielding*

RF shielding is used on the laboratory equipment, but usage of RF shielding on the DAQ is neglected. Further improvements can include RF shielding around the analog components on the printed circuit board.

# Bibliography


[1] [Online]. Available: https://en.wikipedia.org/wiki/Instrumentation_amplifier

[2] I. Bogie, "Conduction and magnetic signalling in the sea a background review," *The Radio and Electronic Engineer*, vol. 42, no. 10, 1972.

[3] S. Constable, "Review paper instrumentation for marine magnetotelluric and controlled source electromagnetic sounding," *Geophysical Prospecting*, vol. 61, pp. 505–532, 2013.

[4] P. Holtham, I. Jeffery, B. Brooking, and T. Richards, "Electromagnetic signature modeling and reduction," Defense Research Establishment Atlantic, Tech. Rep., 1999.

[5] S. R. Qualls, J. M. Osborn, M. J. Anderson, E. T. Wolbrecht, J. F. Frenzel, D. B. Edwards, and J. R. Canning, "Underwater electric potential measurements using AUVs," in *Oceans*, 2015, pp. 1–4.

[6] M. Slater and A. Schultz, "Electromagnetic field study," Oregon Wave Energy Trust (OWET), Tech. Rep., 2010.

[7] L. Crona and A. Brage, "Carbon fibre electrodes and their qualities in salt water," in *Proc. MARELEC 97: Int. Conf. on Marine Electromagnetics*, 1997.

[8] G. B. Havsgard, H. R. Jensen, and A. Kurrasch, "Low noise Ag/AgCl electric field sensor system for marine CSEM and MT applications," in *7th International Marine Electromagnetics MARELEC Conference*, 2011.

[9] S. C. Webb, S. C. Constable, C. S. Cox, and T. K. Deaton, "A seafloor electric field instrument," *Journal of Geomagnetism and Geoelectricity*, vol. 37, no. 12, pp. 1115–1129, 1985.

[10] B. Armstrong, J. Pentzer, D. Odell, T. Bean, J. Canning, D. Pugsley, J. Frenzel, M. Anderson, and D. Edwards, "Field measurement of surface ship magnetic signature using multiple AUVs," in *Proceedings of Oceans 2009 MTS/IEEE*, 2009.

[11] Z. Wang, M. Deng, K. Chen, and M. Wang, "An ultralow-noise Ag/AgCl electric field sensor with good stability for marine EM applications," in *Seventh International Conference on Sensing Technology*, 2013.

[12] W. Instruments. [Online]. Available: https://www.warneronline.com/Documents/uploader/Warner_2011_641304%20E200.pdf

[13] B. J. Polk, A. Stelzenmuller, G. Mijares, W. MacCrehan, and M. Gaitan, "Ag/AgCl microelectrodes with improved stability for microfluidics," *Sensors and Actuators B, Chemical*, 2006.

[14] A. I. Al-Shamma'a, A. Shaw, and S. Saman, "Propagation of electromagnetic waves at MHz frequencies through seawater," *IEEE Transactions on Antennas and Propagation*, vol. 52, no. 11, 2004.

[15] J. Coulon, "A low power low noise instrumenation amplifier for ECG recording applications," Master's thesis, Texas A&M University, 2012.

[16] A. Devices, "Chopper stabilized (auto-zero) precision op amps," Analog Devices, Tech. Rep., 2009.

[17] [Online]. Available: http://www.ti.com/lit/ds/symlink/ina129.pdf

[18] [Online]. Available: http://www.ti.com/lit/ds/sbos445c/sbos445c.pdf

[19] M. Santora and R. Oare, "Modular low-power, low-noise, low-cost wirelessly networked data acquisition system," in *IEEE Oceans*, 2016.

[20] M. Benghanem, "Measurement of meteorological data based on wireless data acquisition system monitoring," *Applied Energy*, 2009.

[21] A. Mahjoubi, R. F. Mechlouch, and A. B. Brahim, "A low cost wireless data acquisition system for a remote photovoltaic (PV) water pumping system," *Energies*, 2011.

[22] R. Morais, J. B. Cunha, M. Cordeiro, C. Serodio, P. Salgado, and C. Couto, "Solar data acquisition wireless network for agricultural applications," *Electrical and Electronics Engineers in Israel*, 1996.

[23] Z. Qian, Y. Xiang-long, Z. Yi-ming, W. Li-ren, and G. Xi-shan, "A wireless solution for greenhouse monitoring and control system based on zigbee technology," *Journal of Zhejiang University*, 2007.

[24] M. Santora and R. Oare, "Methodology for electric potential sensor noise measurements in salt water," in *IEEE Oceans*, 2016.

[25] [Online]. Available: https://communities.intel.com/thread/100706?start=15&tstart=0

[26] D. LaFontaine, "Making accurate voltage noise and current noise measurements on operational amplifiers down to 0.1Hz," Intersil, Tech. Rep., 2011.

[27] H. Schmid, "How to use the FFT and Matlab's pwelch function for signal and noise simulations and measurements," *FHNW/IME*, 2012.

[28] A. W. Hassel, K. Fushimi, and M. Seo, "An agar-based silver|silver chloride reference electrode for use in micro-electrochemistry," *Electrochemistry Communications*, 1999.

[29] F. J. Harris, "Windows, harmonic analysis, and the discrete fourier transform," Naval Undersea Center, Tech. Rep., 1976.

[30] Z. Wang, M. Deng, K. Chen, M. Wang, Q. Zhang, and D. Zeng, "Development and evaluation of an ultralow-noise sensor system for marine electric field measurements," *Sensors and Actuators A, Physical*, vol. 213, pp. 70–78, 2014.

[31] J. M. Osborn, "AUV state estimation, navigation, and control in the presence of ocean currents," Master's thesis, University of Idaho, 2016.

APPENDIX A

# Data Acquisition System Schematic

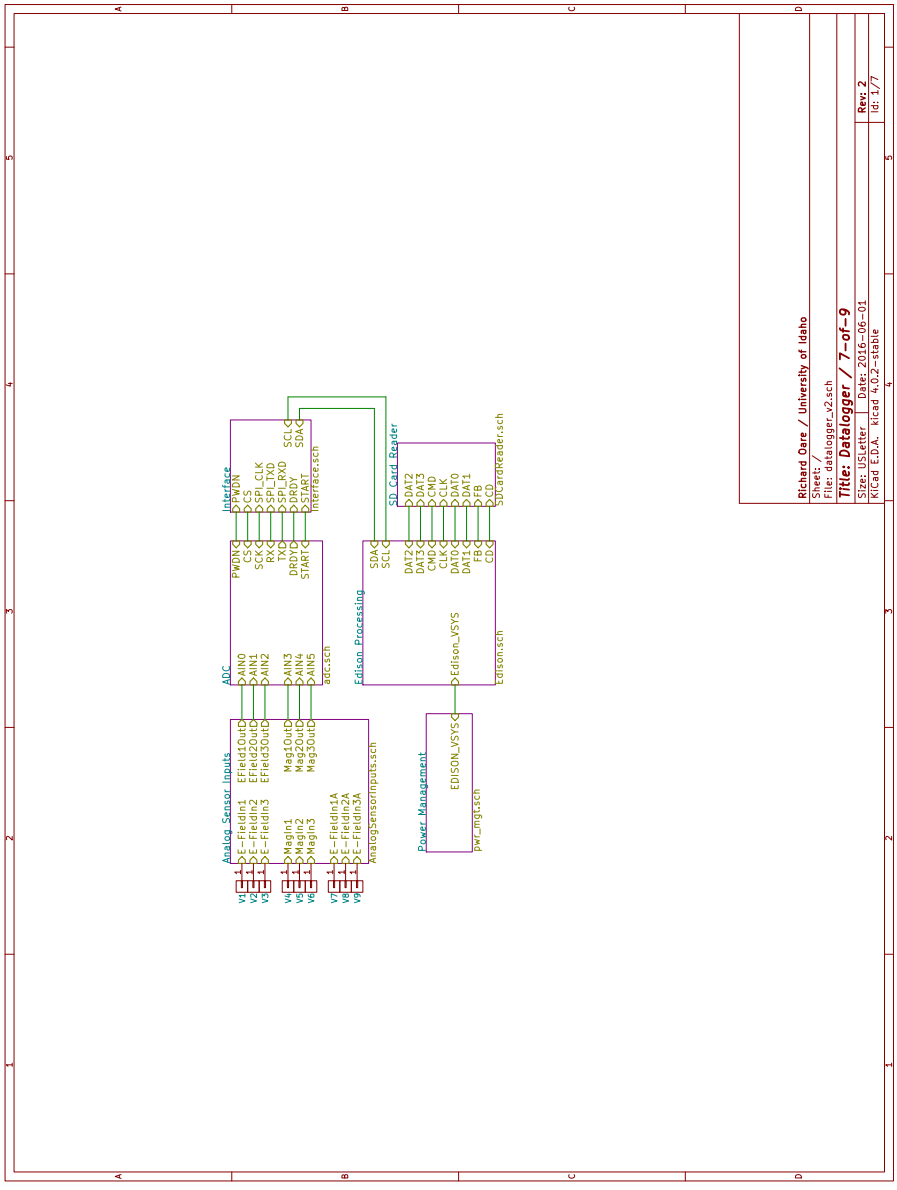


FIGURE A.1: Overall System Connections

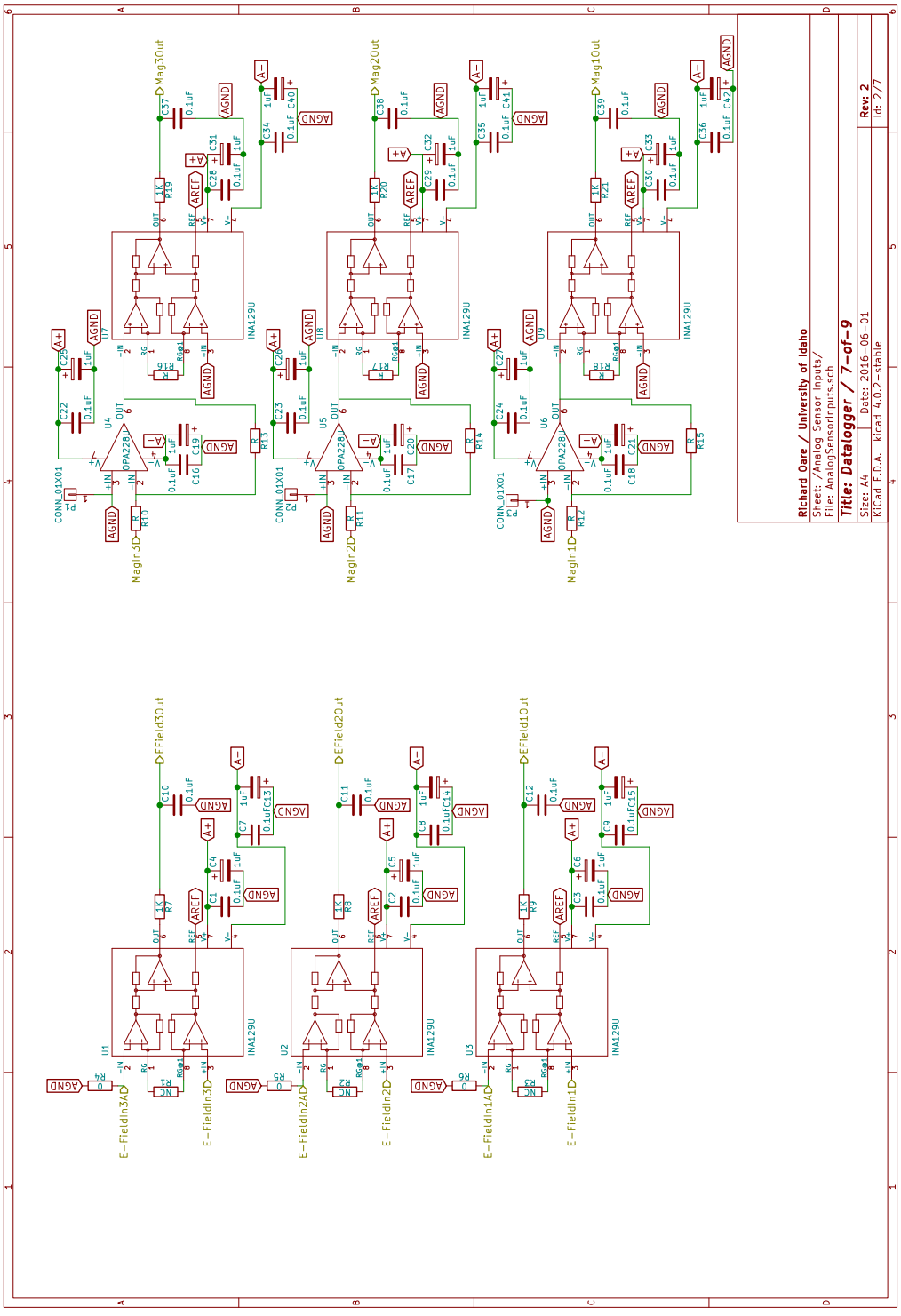


FIGURE A.2: Analog Input Signal Conditioning

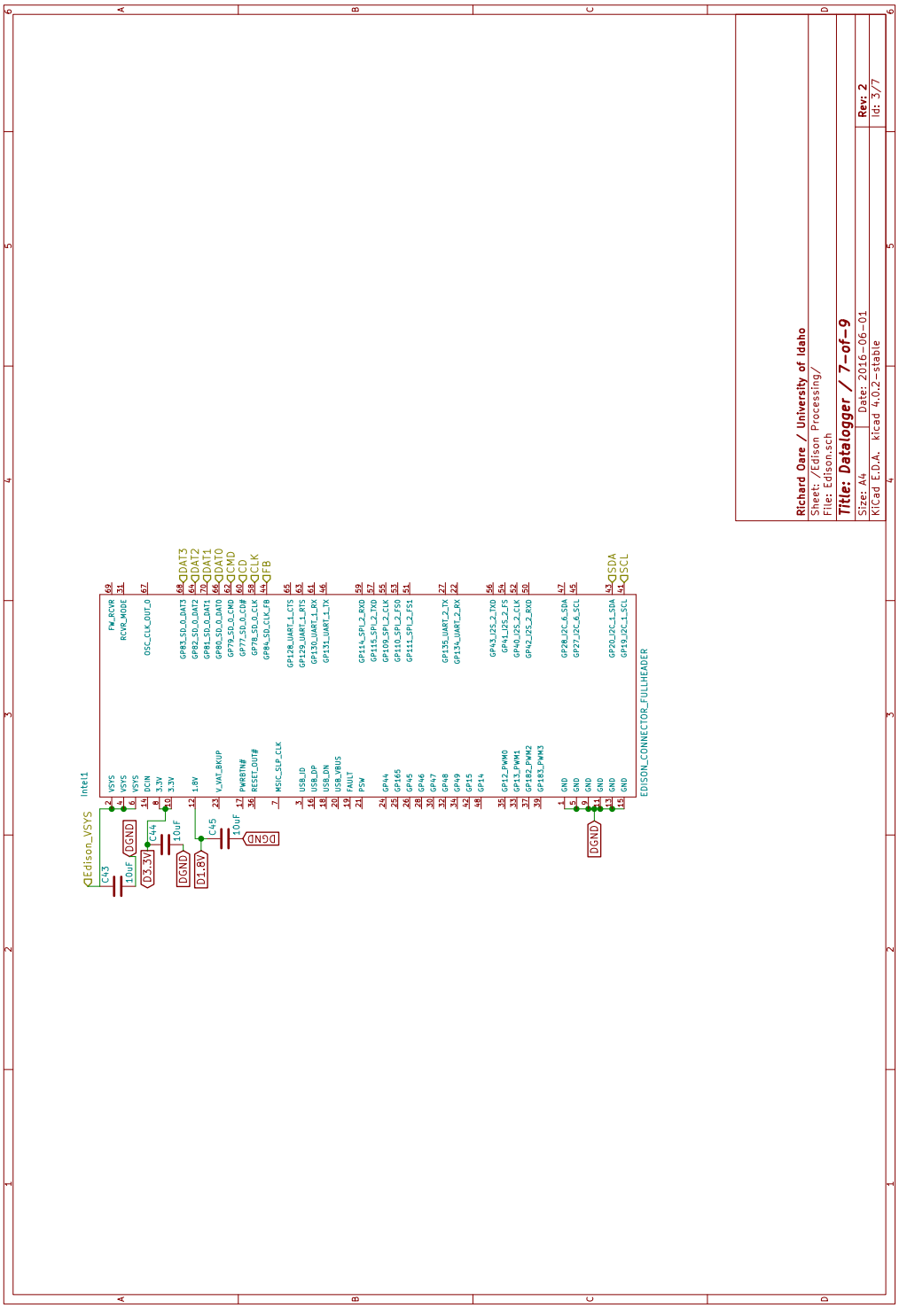


FIGURE A.3: Edison Microprocessor Connections

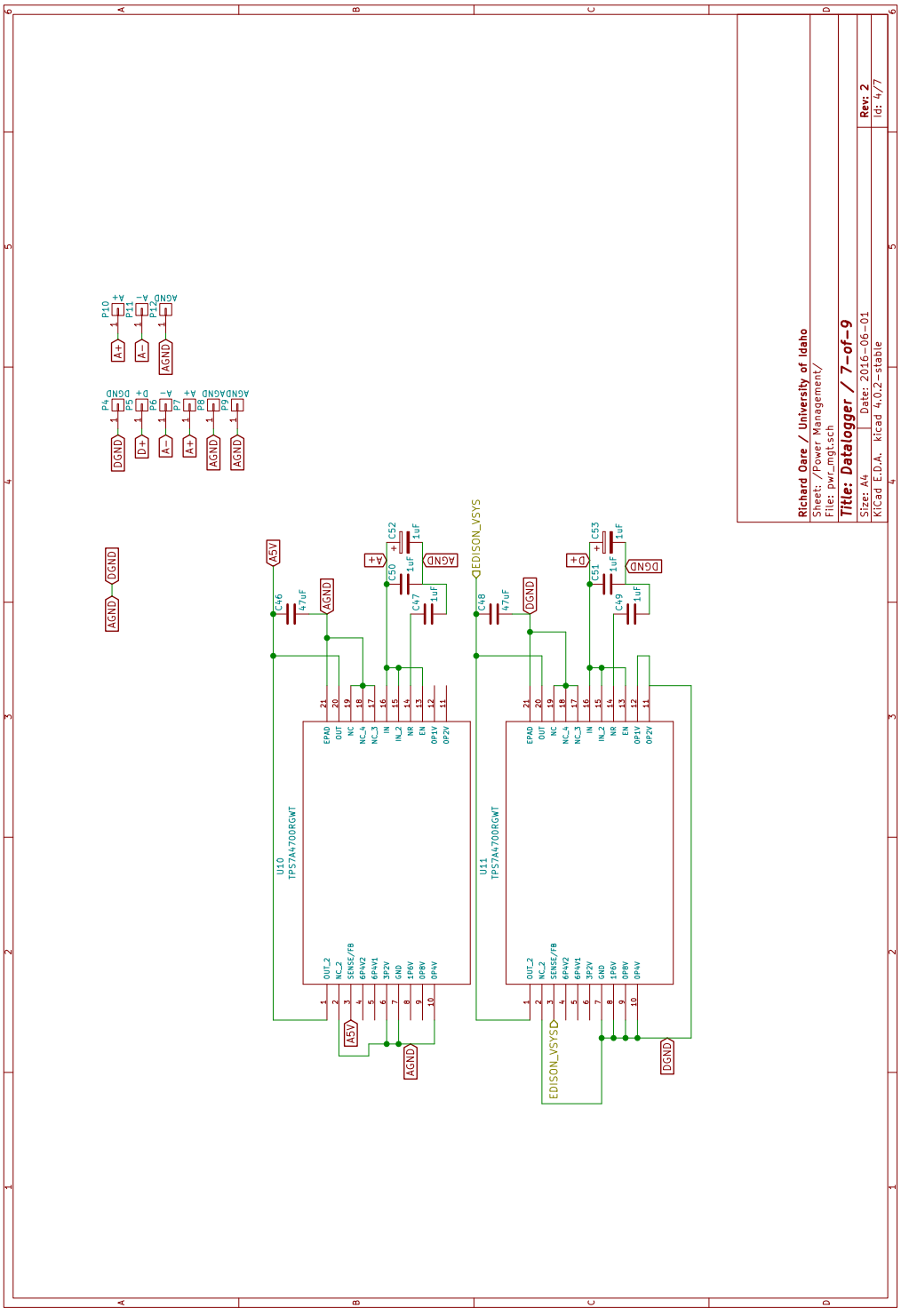


FIGURE A.4: Power Management Circuitry

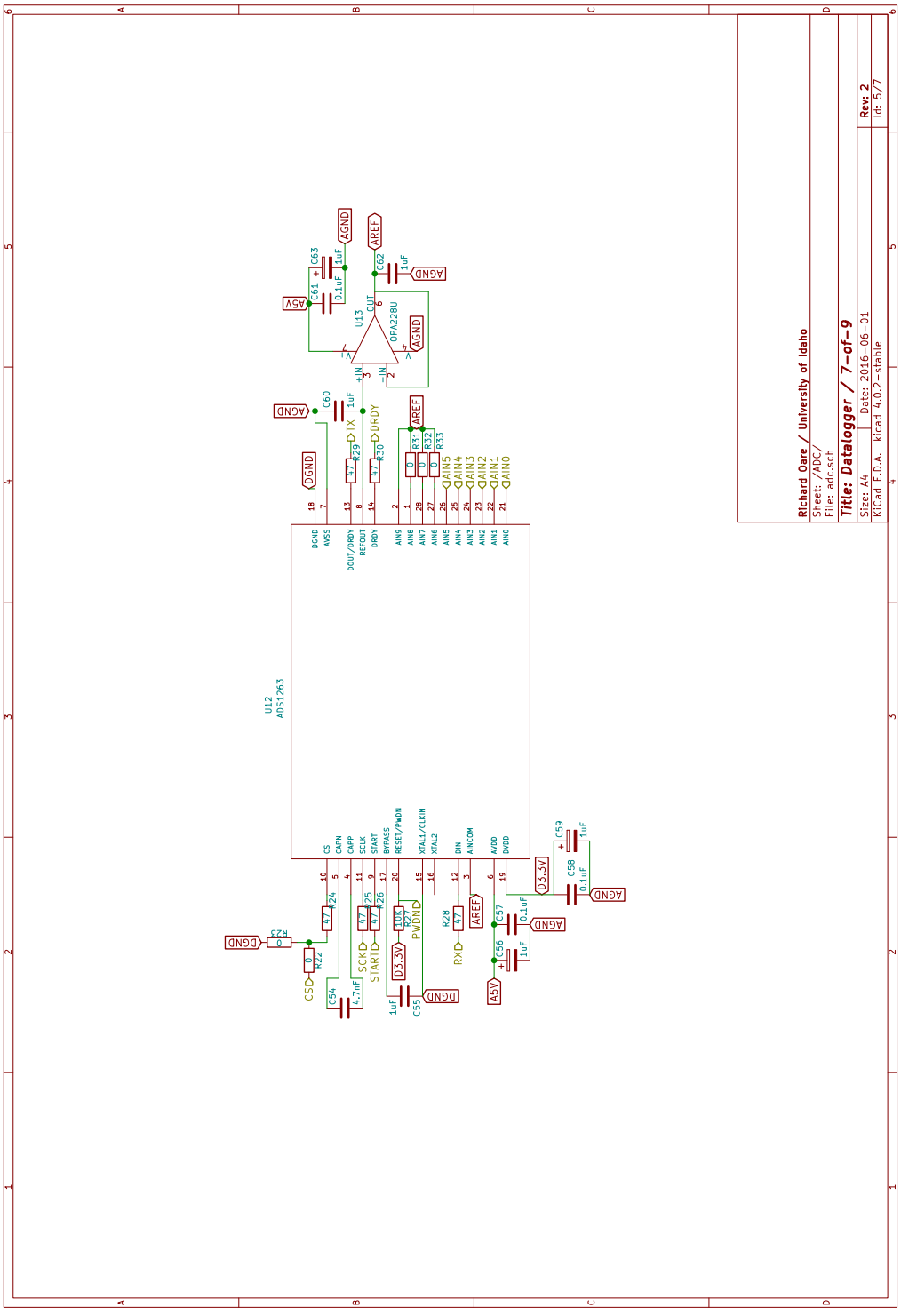


FIGURE A.5: Analog to Digital Converter Circuitry

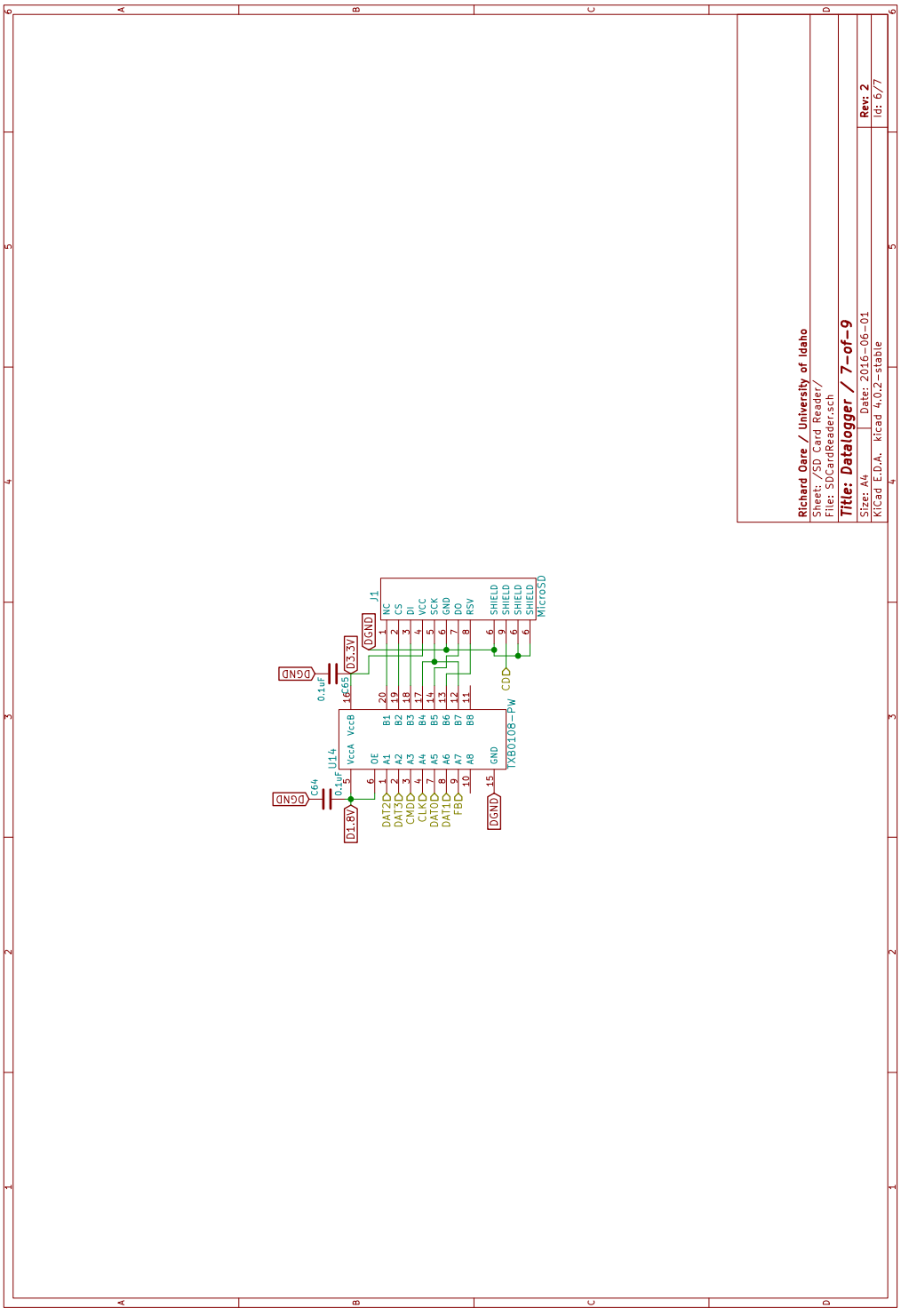


FIGURE A.6: SD Card Circuitry

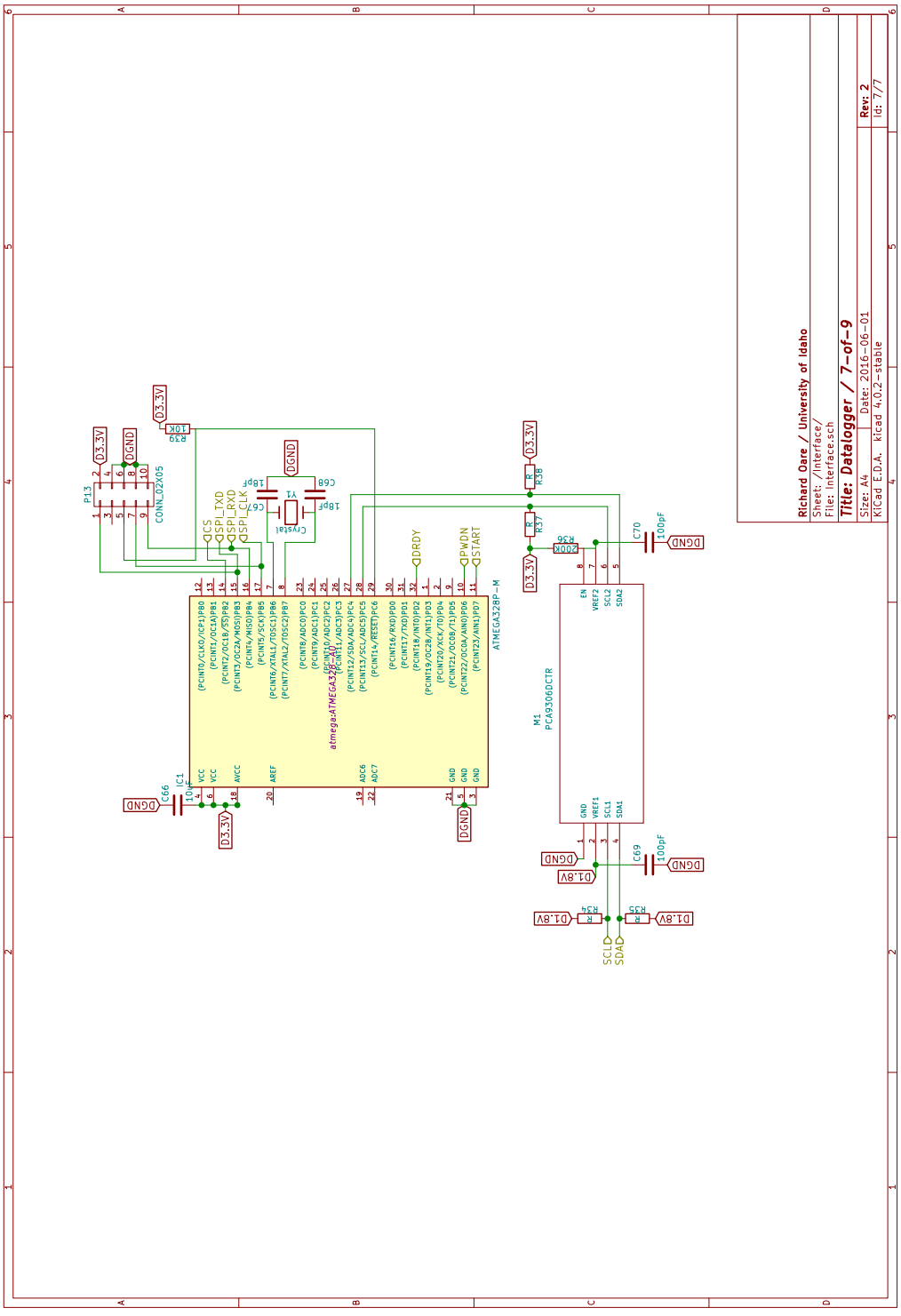


FIGURE A.7: Atmel Microcontroller Interface Circuitry

APPENDIX B

# Ball Probe Construction

Figure B.1 displays the ball probe configuration. On the 1.5-inch ball probe, the electrode numbers in Figure B.1 correspond to the pin numbers of the Seacon connector. The 3-inch ball probe contains an amplifier; consequently, the electrode numbers in Figure B.1 are connected to the amplifier in the configuration listed in Table B.1.

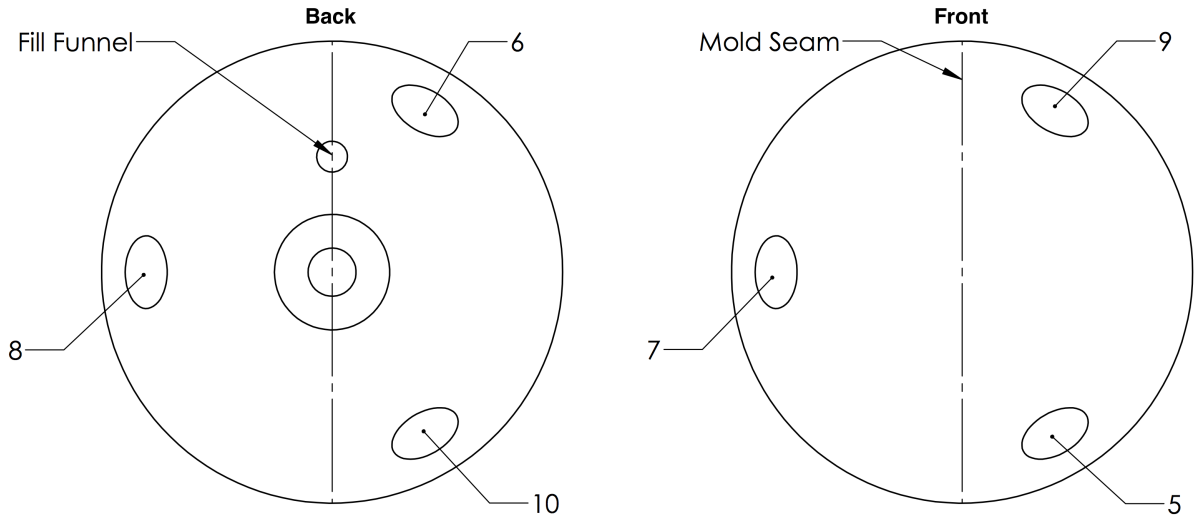


FIGURE B.1: Ball Probe Diagram

TABLE B.1: Electrode Number to Amplifier Input (3-inch Ball Probe)

| Electrode Number | Amplifier Input |
|---|---|
| 5 | U1(+) |
| 6 | U1(-) |
| 7 | U2(+) |
| 8 | U2(-) |
| 9 | U3(+) |
| 10 | U3(-) |

A Category 5 ethernet cable is used for the output from the 3-inch ball probe. The output pin labels to color codes are listed in Table B.2.

TABLE B.2: Amplifier Output to Ethernet Cable

| Amplifier Output | Cat5 Ethernet Cable |
|---|---|
| Ref | Orange Striped, Blue Striped, and Brown Striped |
| V- | Green Striped |
| V+ | Green |
| U1 | Blue |
| U2 | Brown |
| U3 | Orange |

APPENDIX C

# Data Processing Code

```
function [Px,f,retVal] = ampSpectrum ( timeseries , Fs , MinFreq, color, type)
  NFFT = 2^nextpow2 (Fs/MinFreq);
  j = 0:1:NFFT-1;
  ENBW = 3.8112*Fs/NFFT;
  if type == 'hft'
      z = 2*pi*j/NFFT;
      window = 1 - 1.9383379*cos(z) + 1.3045202*cos(2*z) - 0.4028270*cos(3*z) +...
    0.0350665*cos(4*z);
  elseif type == 'h'
      window = hann(NFFT+1);
  elseif type == 'k'
      window = kaiser(NFFT+1);
  end
  detrendedtimeseries = detrend(timeseries);
  [Px,f] = pwelch(detrendedtimeseries, window, NFFT/2 , NFFT, Fs, 'onesided');
  p = loglog(f,sqrt(Px),color);
  retVal = ENBW;
end
```

FIGURE C.1: Matlab Code for Amplitude Spectral Density

```
function [filteredData] = medianFilter(numSamp, data, acceptance)
    filteredData = data;

    a = mean(data(1:numSamp));

    for i = 1:length(data)
        if mod(i,numSamp) == 0
            if length(data) < (i + numSamp)
                x = length(data);
                a = mean(data(i:x));
            else
                x = numSamp;
                a = mean(data(i:i+x));
            end
        end

        if data(i) > (a + acceptance) || data(i) < (a - acceptance)
            filteredData(i) = a;
        end
    end
end
```

FIGURE C.2: Matlab Code for Median Filter

APPENDIX D

# Bill Of Materials

| Reference | Value | Value | Cost | Description | Supplier |
|---|---|---|---|---|---|
| C1 | 0.1uF | 490-1524-1-ND | 0.1 | 0.10$\mu$F 25V Ceramic Capacitor X7R 0603 | Digikey |
| C10 | 0.1uF | 490-1524-1-ND | 0.1 | 0.10$\mu$F 25V Ceramic Capacitor X7R 0603 | Digikey |
| C11 | 0.1uF | 490-1524-1-ND | 0.1 | 0.10$\mu$F 25V Ceramic Capacitor X7R 0603 | Digikey |
| C12 | 0.1uF | 490-1524-1-ND | 0.1 | 0.10$\mu$F 25V Ceramic Capacitor X7R 0603 | Digikey |
| C13 | 1uF | 478-8657-1-ND | 0.7 | 1$\mu$F Molded Tantalum Capacitors 20V 0603 | Digikey |
| C14 | 1uF | 478-8657-1-ND | 0.7 | 1$\mu$F Molded Tantalum Capacitors 20V 0603 | Digikey |
| C15 | 1uF | 478-8657-1-ND | 0.7 | 1$\mu$F Molded Tantalum Capacitors 20V 0603 | Digikey |
| C16 | 0.1uF | 490-1524-1-ND | 0.1 | 0.10$\mu$F 25V Ceramic Capacitor X7R 0603 | Digikey |
| C17 | 0.1uF | 490-1524-1-ND | 0.1 | 0.10$\mu$F 25V Ceramic Capacitor X7R 0603 | Digikey |
| C18 | 0.1uF | 490-1524-1-ND | 0.1 | 0.10$\mu$F 25V Ceramic Capacitor X7R 0603 | Digikey |
| C19 | 1uF | 478-8657-1-ND | 0.7 | 1$\mu$F Molded Tantalum Capacitors 20V 0603 | Digikey |
| C2 | 0.1uF | 490-1524-1-ND | 0.1 | 0.10$\mu$F 25V Ceramic Capacitor X7R 0603 | Digikey |
| C20 | 1uF | 478-8657-1-ND | 0.7 | 1$\mu$F Molded Tantalum Capacitors 20V 0603 | Digikey |
| C21 | 1uF | 478-8657-1-ND | 0.7 | 1$\mu$F Molded Tantalum Capacitors 20V 0603 | Digikey |
| C22 | 0.1uF | 490-1524-1-ND | 0.1 | 0.10$\mu$F 25V Ceramic Capacitor X7R 0603 | Digikey |
| C23 | 0.1uF | 490-1524-1-ND | 0.1 | 0.10$\mu$F 25V Ceramic Capacitor X7R 0603 | Digikey |
| C24 | 0.1uF | 490-1524-1-ND | 0.1 | 0.10$\mu$F 25V Ceramic Capacitor X7R 0603 | Digikey |
| C25 | 1uF | 478-8657-1-ND | 0.7 | 1$\mu$F Molded Tantalum Capacitors 20V 0603 | Digikey |
| C26 | 1uF | 478-8657-1-ND | 0.7 | 1$\mu$F Molded Tantalum Capacitors 20V 0603 | Digikey |
| C27 | 1uF | 478-8657-1-ND | 0.7 | 1$\mu$F Molded Tantalum Capacitors 20V 0603 | Digikey |
| C28 | 0.1uF | 490-1524-1-ND | 0.1 | 0.10$\mu$F 25V Ceramic Capacitor X7R 0603 | Digikey |
| C29 | 0.1uF | 490-1524-1-ND | 0.1 | 0.10$\mu$F 25V Ceramic Capacitor X7R 0603 | Digikey |
| C3 | 0.1uF | 490-1524-1-ND | 0.1 | 0.10$\mu$F 25V Ceramic Capacitor X7R 0603 | Digikey |
| C30 | 0.1uF | 490-1524-1-ND | 0.1 | 0.10$\mu$F 25V Ceramic Capacitor X7R 0603 | Digikey |

| | | | | | |
|---|---|---|---|---|---|
| **C31** | 1uF | 478-8657-1-ND | 0.7 | 1μF Molded Tantalum Capacitors 20V 0603 | Digikey |
| **C32** | 1uF | 478-8657-1-ND | 0.7 | 1μF Molded Tantalum Capacitors 20V 0603 | Digikey |
| **C33** | 1uF | 478-8657-1-ND | 0.7 | 1μF Molded Tantalum Capacitors 20V 0603 | Digikey |
| **C34** | 0.1uF | 490-1524-1-ND | 0.1 | 0.10μF 25V Ceramic Capacitor X7R 0603 | Digikey |
| **C35** | 0.1uF | 490-1524-1-ND | 0.1 | 0.10μF 25V Ceramic Capacitor X7R 0603 | Digikey |
| **C36** | 0.1uF | 490-1524-1-ND | 0.1 | 0.10μF 25V Ceramic Capacitor X7R 0603 | Digikey |
| **C37** | 0.1uF | 490-1524-1-ND | 0.1 | 0.10μF 25V Ceramic Capacitor X7R 0603 | Digikey |
| **C38** | 0.1uF | 490-1524-1-ND | 0.1 | 0.10μF 25V Ceramic Capacitor X7R 0603 | Digikey |
| **C39** | 0.1uF | 490-1524-1-ND | 0.1 | 0.10μF 25V Ceramic Capacitor X7R 0603 | Digikey |
| **C4** | 1uF | 478-8657-1-ND | 0.7 | 1μF Molded Tantalum Capacitors 20V 0603 | Digikey |
| **C40** | 1uF | 478-8657-1-ND | 0.7 | 1μF Molded Tantalum Capacitors 20V 0603 | Digikey |
| **C41** | 1uF | 478-8657-1-ND | 0.7 | 1μF Molded Tantalum Capacitors 20V 0603 | Digikey |
| **C42** | 1uF | 478-8657-1-ND | 0.7 | 1μF Molded Tantalum Capacitors 20V 0603 | Digikey |
| **C43** | 10uF | 490-12737-1-ND | 0.36 | 10μF 25V Ceramic Capacitor X5R 0603 | Digikey |
| **C44** | 10uF | 490-12737-1-ND | 0.36 | 10μF 25V Ceramic Capacitor X5R 0603 | Digikey |
| **C45** | 10uF | 490-12737-1-ND | 0.36 | 10μF 25V Ceramic Capacitor X5R 0603 | Digikey |
| **C46** | 47uF | 1276-6823-1-ND | 0.52 | 47μF 6.3V Ceramic Capacitor X5R 0603 | Digikey |
| **C47** | 1uF | 490-3897-1-ND | 0.1 | 1μF 25V Ceramic Capacitor X5R 0603 | Digikey |
| **C48** | 47uF | 1276-6823-1-ND | 0.52 | 47μF 6.3V Ceramic Capacitor X5R 0603 | Digikey |
| **C49** | 1uF | 490-3897-1-ND | 0.1 | 1μF 25V Ceramic Capacitor X5R 0603 | Digikey |
| **C5** | 1uF | 478-8657-1-ND | 0.7 | 1μF Molded Tantalum Capacitors 20V 0603 | Digikey |
| **C50** | 1uF | 490-3897-1-ND | 0.1 | 1μF 25V Ceramic Capacitor X5R 0603 | Digikey |
| **C51** | 1uF | 490-3897-1-ND | 0.1 | 1μF 25V Ceramic Capacitor X5R 0603 | Digikey |
| **C52** | 1uF | 478-8657-1-ND | 0.7 | 1μF Molded Tantalum Capacitors 20V 0603 | Digikey |
| **C53** | 1uF | 478-8657-1-ND | 0.7 | 1μF Molded Tantalum Capacitors 20V 0603 | Digikey |
| **C54** | 4.7nF | 399-9087-1-ND | 1.35 | 4700pF 25V Ceramic Capacitor C0G, NP0 0603 | Digikey |

| | | | | | |
|---|---|---|---|---|---|
| **C55** | 1uF | 490-3897-1-ND | 0.1 | 1$\mu$F 25V Ceramic Capacitor X5R 0603 | Digikey |
| **C56** | 1uF | 478-8657-1-ND | 0.7 | 1$\mu$F Molded Tantalum Capacitors 20V 0603 | Digikey |
| **C57** | 0.1uF | 490-1524-1-ND | 0.1 | 0.10$\mu$F 25V Ceramic Capacitor X7R 0603 | Digikey |
| **C58** | 0.1uF | 490-1524-1-ND | 0.1 | 0.10$\mu$F 25V Ceramic Capacitor X7R 0603 | Digikey |
| **C59** | 1uF | 478-8657-1-ND | 0.7 | 1$\mu$F Molded Tantalum Capacitors 20V 0603 | Digikey |
| **C6** | 1uF | 478-8657-1-ND | 0.7 | 1$\mu$F Molded Tantalum Capacitors 20V 0603 | Digikey |
| **C60** | 1uF | 490-3897-1-ND | 0.1 | 1$\mu$F 25V Ceramic Capacitor X5R 0603 | Digikey |
| **C61** | 0.1uF | 490-1524-1-ND | 0.1 | 0.10$\mu$F 25V Ceramic Capacitor X7R 0603 | Digikey |
| **C62** | 1uF | 490-3897-1-ND | 0.1 | 1$\mu$F 25V Ceramic Capacitor X5R 0603 | Digikey |
| **C63** | 1uF | 478-8657-1-ND | 0.7 | 1$\mu$F Molded Tantalum Capacitors 20V 0603 | Digikey |
| **C64** | 0.1uF | 490-1524-1-ND | 0.1 | 0.10$\mu$F 25V Ceramic Capacitor X7R 0603 | Digikey |
| **C65** | 0.1uF | 490-1524-1-ND | 0.1 | 0.10$\mu$F 25V Ceramic Capacitor X7R 0603 | Digikey |
| **C66** | 10uF | 490-12737-1-ND | 0.36 | 10$\mu$F 25V Ceramic Capacitor X5R 0603 | Digikey |
| **C67** | 18pF | 399-8828-1-ND | 0.34 | 18pF 50V Ceramic Capacitor C0G, NP0 0402 | Digikey |
| **C68** | 18pF | 399-8828-1-ND | 0.34 | 18pF 50V Ceramic Capacitor C0G, NP0 0402 | Digikey |
| **C69** | 100pF | 399-1061-1-ND | 0.1 | 100pF 50V Ceramic Capacitor C0G, NP0 0603 | Digikey |
| **C7** | 0.1uF | 490-1524-1-ND | 0.1 | 0.10$\mu$F 25V Ceramic Capacitor X7R 0603 | Digikey |
| **C70** | 100pF | 399-1061-1-ND | 0.1 | 100pF 50V Ceramic Capacitor C0G, NP0 0603 | Digikey |
| **C8** | 0.1uF | 490-1524-1-ND | 0.1 | 0.10$\mu$F 25V Ceramic Capacitor X7R 0603 | Digikey |
| **C9** | 0.1uF | 490-1524-1-ND | 0.1 | 0.10$\mu$F 25V Ceramic Capacitor X7R 0603 | Digikey |
| **IC1** | ATMEGA328P-M | ATMEGA328P-AURCT-ND | 3.81 | Atmel Atmega328p Microcontroller | Digikey |
| **Intel1** | EDISON_CONNECTOR_FULLHEADER | 798-DF40HC3070DS4V51 | 2.25 | Board to Board & Mezzanine Connectors 70P RECPT 3.0 | Mouser |
| **J1** | MicroSD | WM3295CT-ND | 10.77 | MicroSD Card Slot | Digikey |
| **M1** | PCA9306DCTR | 296-27957-1-ND | 0.79 | Texas Instruments PCA9306 | Digikey |
| **P13** | CONN_02X05 | | 0.139 | 2.54mm Straight Male IDC Socket Box header connector | Ebay |
| **R10** | R | | | | |

| | | | | | |
|---|---|---|---|---|---|
| **R11** | R | | | | |
| **R12** | R | | | | |
| **R13** | R | | | | |
| **R14** | R | | | | |
| **R15** | R | | | | |
| **R19** | 1K | RG16P1.0KBCT-ND | 0.4 | RES SMD 1K OHM 0.1% 1/10W 0603 | Digikey |
| **R20** | 1K | RG16P1.0KBCT-ND | 0.4 | RES SMD 1K OHM 0.1% 1/10W 0603 | Digikey |
| **R21** | 1K | RG16P1.0KBCT-ND | 0.4 | RES SMD 1K OHM 0.1% 1/10W 0603 | Digikey |
| **R22** | 0 | 311-0.0GRCT-ND | 0.1 | RES SMD 0.0OHM JUMPER 1/10W 0603 | Digikey |
| **R23** | 0 | 311-0.0GRCT-ND | 0.1 | RES SMD 0.0OHM JUMPER 1/10W 0603 | Digikey |
| **R24** | 47 | 311-47GRCT-ND | 0.1 | RES SMD 47 OHM 5% 1/10W 0603 | Digikey |
| **R25** | 47 | 311-47GRCT-ND | 0.1 | RES SMD 47 OHM 5% 1/10W 0603 | Digikey |
| **R26** | 47 | 311-47GRCT-ND | 0.1 | RES SMD 47 OHM 5% 1/10W 0603 | Digikey |
| **R27** | 10K | 311-10.0KHRCT-ND | 0.1 | RES SMD 10K OHM 1% 1/10W 0603 | Digikey |
| **R28** | 47 | 311-47GRCT-ND | 0.1 | RES SMD 47 OHM 5% 1/10W 0603 | Digikey |
| **R29** | 47 | 311-47GRCT-ND | 0.1 | RES SMD 47 OHM 5% 1/10W 0603 | Digikey |
| **R30** | 47 | 311-47GRCT-ND | 0.1 | RES SMD 47 OHM 5% 1/10W 0603 | Digikey |
| **R31** | 0 | 311-0.0GRCT-ND | 0.1 | RES SMD 0.0OHM JUMPER 1/10W 0603 | Digikey |
| **R32** | 0 | 311-0.0GRCT-ND | 0.1 | RES SMD 0.0OHM JUMPER 1/10W 0603 | Digikey |
| **R33** | 0 | 311-0.0GRCT-ND | 0.1 | RES SMD 0.0OHM JUMPER 1/10W 0603 | Digikey |
| **R34** | R | | | | Digikey |
| **R35** | R | | | | Digikey |
| **R36** | 200K | 311-200KGRCT-ND | 0.1 | RES SMD 200K OHM 5% 1/10W 0603 | Digikey |
| **R37** | R | | | | Digikey |
| **R38** | R | | | | Digikey |
| **R39** | 10K | 311-10.0KHRCT-ND | 0.1 | RES SMD 10K OHM 1% 1/10W 0603 | Digikey |

| | | | | | |
|---|---|---|---|---|---|
| **R4** | 0 | 311-0.0GRCT-ND | 0.1 | RES SMD 0.0OHM JUMPER 1/10W 0603 | Digikey |
| **R5** | 0 | 311-0.0GRCT-ND | 0.1 | RES SMD 0.0OHM JUMPER 1/10W 0603 | Digikey |
| **R6** | 0 | 311-0.0GRCT-ND | 0.1 | RES SMD 0.0OHM JUMPER 1/10W 0603 | Digikey |
| **R7** | 1K | RG16P1.0KBCT-ND | 0.4 | RES SMD 1K OHM 0.1% 1/10W 0603 | Digikey |
| **R8** | 1K | RG16P1.0KBCT-ND | 0.4 | RES SMD 1K OHM 0.1% 1/10W 0603 | Digikey |
| **R9** | 1K | RG16P1.0KBCT-ND | 0.4 | RES SMD 1K OHM 0.1% 1/10W 0603 | Digikey |
| **U1** | INA129U | 296-26058-1-ND | 7.2 | Texas Instruments INA129U | Digikey |
| **U10** | TPS7A4700RGWT | 296-39503-1-ND | 4.79 | Texas Instruments TPS7A4700 | Digikey |
| **U11** | TPS7A4700RGWT | 296-39503-1-ND | 4.79 | Texas Instruments TPS7A4700 | Digikey |
| **U12** | ADS1263 | 296-42485-1-ND | 22.66 | Texas Instruments ADS1263 | Digikey |
| **U13** | OPA228U | OPA228UA-ND | 3.29 | Texas Instruments OPA228U | Digikey |
| **U14** | TXB0108-PW | 296-27217-1-ND | 1.88 | Texas Instruments TXB0108 | Digikey |
| **U2** | INA129U | 296-26058-1-ND | 7.2 | Texas Instruments INA129U | Digikey |
| **U3** | INA129U | 296-26058-1-ND | 7.2 | Texas Instruments INA129U | Digikey |
| **U4** | OPA228U | OPA228UA-ND | 3.29 | Texas Instruments OPA228U | Digikey |
| **U5** | OPA228U | OPA228UA-ND | 3.29 | Texas Instruments OPA228U | Digikey |
| **U6** | OPA228U | OPA228UA-ND | 3.29 | Texas Instruments OPA228U | Digikey |
| **U7** | INA129U | 296-26058-1-ND | 7.2 | Texas Instruments INA129U | Digikey |
| **U8** | INA129U | 296-26058-1-ND | 7.2 | Texas Instruments INA129U | Digikey |
| **U9** | INA129U | 296-26058-1-ND | 7.2 | Texas Instruments INA129U | Digikey |
| **Y1** | Crystal | 887-1265-1-ND | 0.59 | 10MHz ±10ppm Crystal 18pF 40 Ohm Surface Mount | Digikey |
| **Intel Edison** | Intel Edison | DEV-13024 | 50 | Intel Edison | sparkfun |
| | | Total Cost: | 187.339 | | |

APPENDIX E

# Radio Frequency (RF) Noise

The 1.5-inch ball probe includes long lead wires to the amplifier which pick up surrounding radio frequency (RF) noise. This noise is then amplified and supplied to the data acquisition device (DAQ). This test shows those effects and how RF shielding solves the issue. RF shielding in the case of the ball probe includes placing the amplifier as close to the electrodes as possible, as is with the 3-inch ball probe. The surrounding water is then used to isolate the signal on the electrodes from noise sources.

## E.1 TEST SETUP

Test cases are developed as shown in Figures E.1, E.2, and E.3, where 'V' denotes the points where input and output voltage data is collected. The circuit diagram for the amplifier without modification is shown in Figure E.1, the circuit diagram with a low-pass RC filter on the input is shown in Figure E.2, and the circuit diagram for the amplifier where the red dashed box represents the area covered by RF shielding is illustrated in Figure E.3. The actual setup for the amplifier with RF shielding, metal box, is displayed in Figure E.4. The National Instruments NI 9239 is used in this testing.

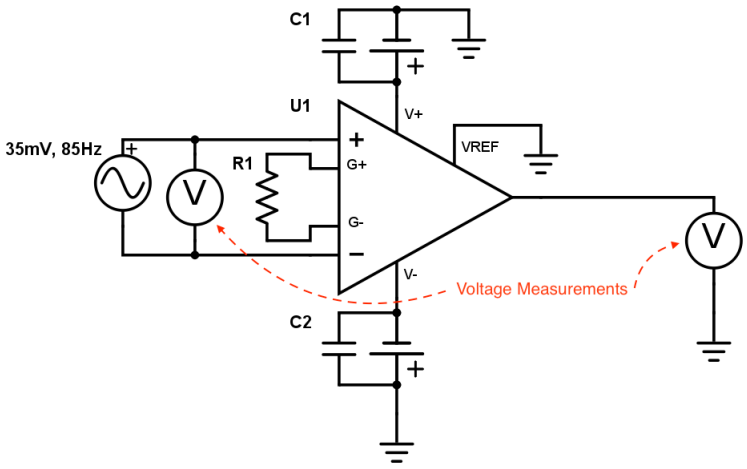


FIGURE E.1: Amplifier with No Modifications

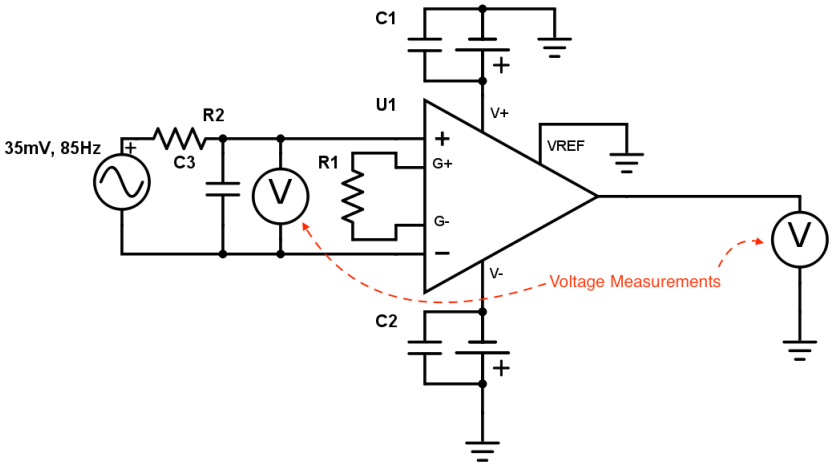


FIGURE E.2: Low-Pass RC Filtered Input to the Amplifier

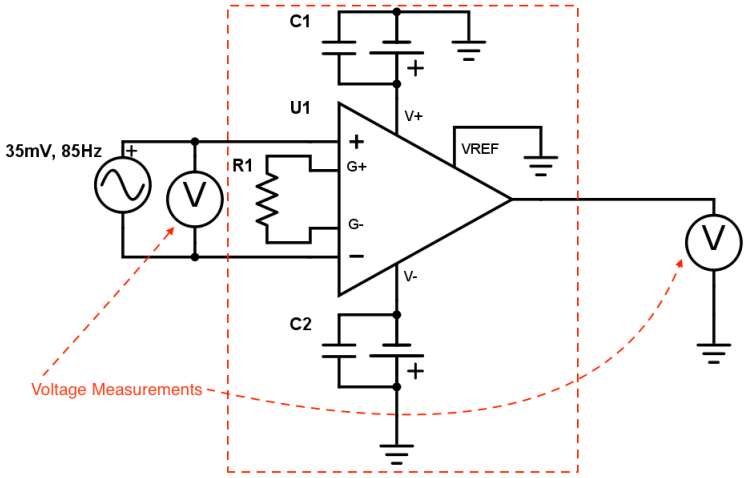


FIGURE E.3: RF Shielded Amplifier (Red-Dashed Box Represents Area Covered by RF Shielding)

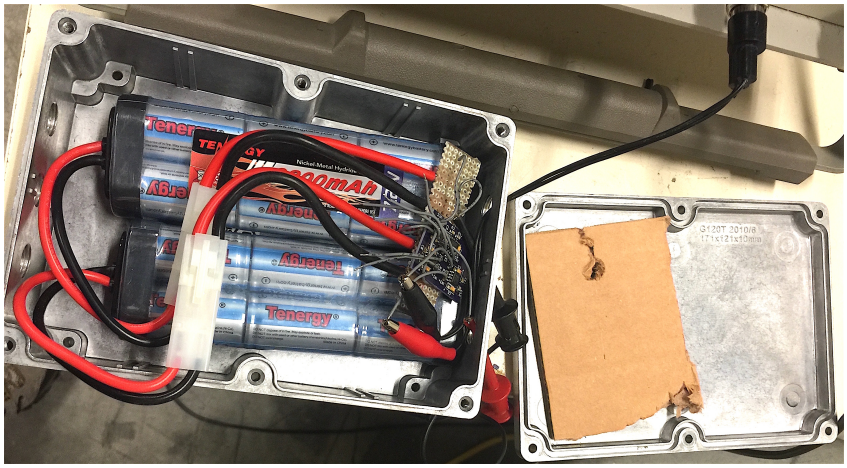

FIGURE E.4: RF Shielding Box Containing Amplifier and Batteries

## E.2 TEST RESULTS

It can be seen from Figures E.5, E.6, and E.7 that the input signals to each test case appear unaltered; however, there is high frequency RF noise on the signals. The NI 9239 filters these high frequency components with an attenuation of 100 $dB$. This filtering allows the input signals to appear noise free, but when the signal and noise is amplified by 48 $dB$, enough high frequency noise passes through such that aliased components appear on the output. This noise shows up as a distortion as shown in

Figure E.8. With a low-pass filter or RF shielding, a clean output can appear as shown in Figure E.9 and Figure E.10.

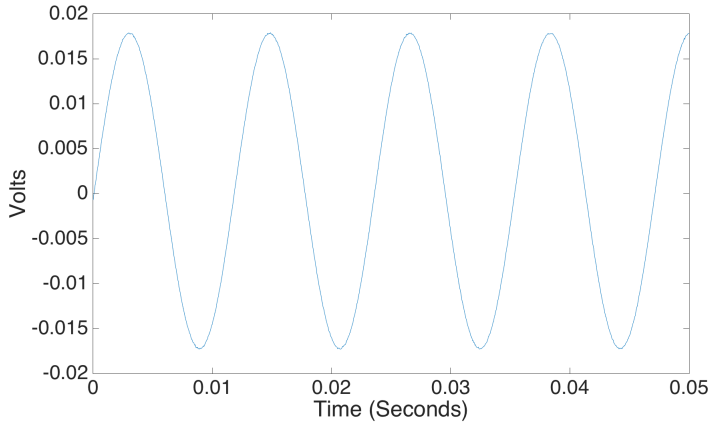


FIGURE E.5: Signal Input to the Amplifier (No Filtering)

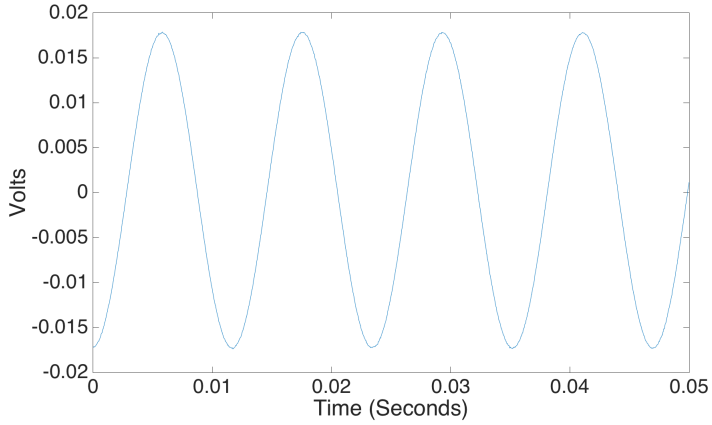


FIGURE E.6: Signal Input to the Amplifier (RC Filtering)

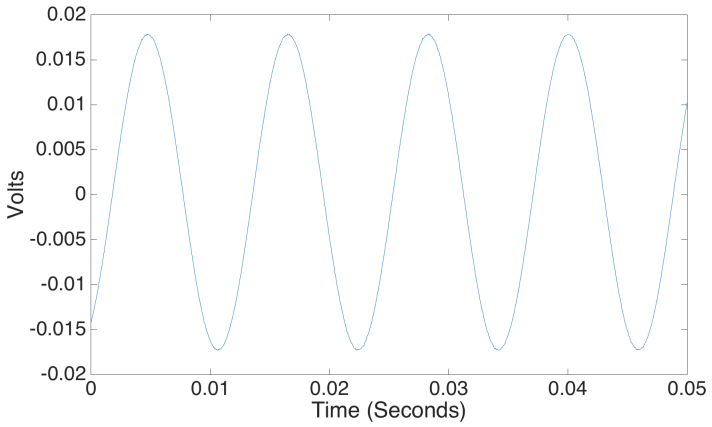


FIGURE E.7: Signal Input to the Amplifier (RF Shielding)

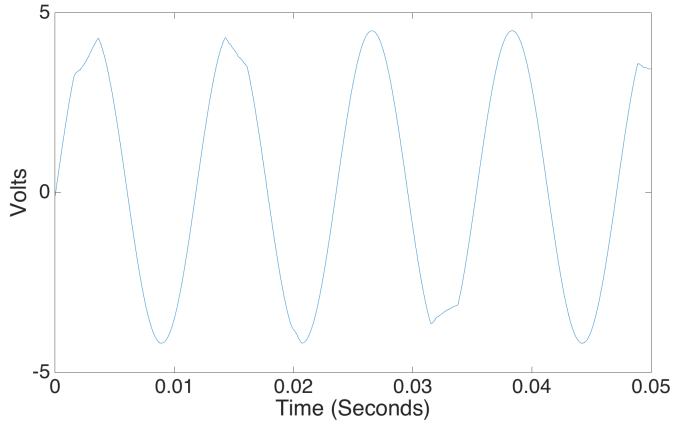


FIGURE E.8: Signal Output from Amplifier (No Filtering)

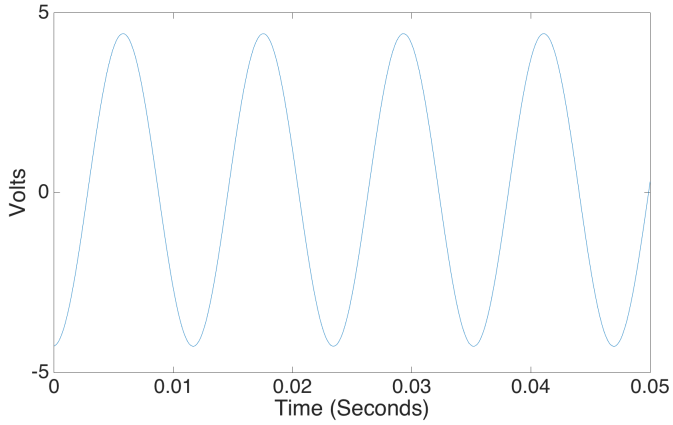


FIGURE E.9: Signal Output from Amplifier (RC Filtering)

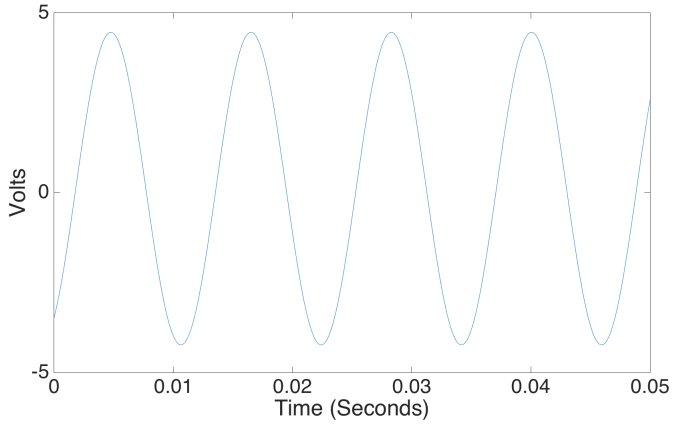


FIGURE E.10: Signal Output from Amplifier (RF Shielding)